# Nonperturbative wave packet dynamics of the photodissociation of H2 + in ultrashort laser pulses

Hakima AbouRachid, T. Tung NguyenDang, Rajat K. Chaudhury, and Xin He

## Articles you may be interested in

# Nonperturbative wave packet dynamics of the photodissociation of $H_2^+$ in ultrashort laser pulses

Hakima Abou-Rachid, T. Tung Nguyen-Dang,[a] Rajat K. Chaudhury, and Xin He

*Départment de Chimie, Faculté des Sciences et de Génies, Université Laval, Québec, G1K 7P4, P.Q., Canada*

The wave packet dynamics of the photodissociation of $H_2^+$ under excitation by laser pulses of short durations at 329.7 nm are studied. The photodissociation process involves essentially two coupled channels, and the detailed mechanism for the formation of fragment kinetic energy spectra is examined by following the evolution of structures in the coupled-channel wave functions in momentum space. These structures appear in the channels' momentum wave functions at $P \neq 0$, as the $v=0$ ground vibrational state is promoted to the dissociative channel then accelerated. The variations of these structures reflect the interplay between local laser-induced transitions and the accelerating–decelerating action of intrinsic molecular forces. The wave packet dynamics are studied for rectangular and Gaussian pulses of varying durations and peak intensities. In addition, two forms of channel couplings were considered corresponding to two different choices of the gauge: the electric-field (EF) gauge, in which the matter–field interaction is of the length form and the radiation-field (RF) gauge, in which it is of the velocity form.

## I. INTRODUCTION

Ultrashort laser pulses allow the time-resolved details of the dynamics of molecular systems to be monitored and they are being used as tools to probe local forces that govern intramolecular energy transfers in the course of the fragmentation of molecules prepared in a dissociative excited state.[1-3] Understanding the effects of the high intensities delivered by short laser pulses and of the pulse shape variations is central to the understanding of the control of molecular processes obtained by tailoring laser pulses.[4,5] The high intensities of present-day lasers have led to indepth revisions of our concept of molecule–radiation interactions. Previous theoretical efforts have been focused mostly on the high-intensity effects on the molecular dynamics and assumed either an ever-present quantized field[6-13] or a classical continuous-wave (cw) periodic field.[14,15] These assumptions allow a time-independent stationary-state description to be used, in what is now known as the dressed molecule or Floquet representation.

In the strictest sense, the dressed molecule or Floquet representation is only useful if the laser is continuous, as in this case, time evolution from an arbitrary initial state can always be expressed in terms of a superposition of the stationary eigenstates of the dressed or Floquet Hamiltonian. A recent study of the photodissociation of $H_2^+$ in intense fields has demonstrated the numerical equivalence between this stationary-state description of the dynamics and a direct time-dependent treatment in the case of a field that is essentially continuous.[16,17] The stationary dressed molecule representation becomes less attractive for excitation by a short pulsed laser. Modulations of the field amplitude in time cannot be incorporated easily into the quantized-field formalism or in the classical Floquet formalism since these intrinsically assume an ever-present periodic field. An artifice such as the assumption of adiabatic transport of Floquet states[18,19] is needed. The Floquet states which depend parametrically on the modulated field amplitude can also be viewed as defining an adiabatic basis in which the time evolution of the laser-driven molecular system involves nonadiabatic couplings which become stronger as the laser pulse gets shorter.[20]

The impetus for extending the dressed molecule picture to the case of excitation by a short pulse is to be found in the interpretative power of this picture, in which multiphoton processes are viewed as laser-induced curve-crossing processes. Thus the structured proton kinetic energy spectra observed, when $H_2^+$ is dissociated in the presence of relatively long and intense laser pulses, have been successfully interpreted in terms of dressed-potential energy surfaces and their deformations by the field intensity.[21,22] A few recent theoretical studies of photodissociation under excitations by shorter pulses solve the time-dependent Schrödinger equation directly to generate and propagate wave packets on the two coupled channels but these studies still rely on the dressed-potential energy surfaces derived from the cw stationary-state description to interpret the results.[23,24] For relatively long pulses, very recent wave packet calculations show a stabilization of the molecule with respect to the photodissociation,[25] in agreement with a prediction which was made previously on the basis of properties of laser-induced resonances described within the dressed-molecule picture.[10] Aside from the use of concepts derived from the time-independent descriptions, the interpretation using the dressed-molecule picture, such as found in Ref. 24, overemphasizes resonant laser-induced transitions between the two channels. The roles played by nonresonant processes and intrinsic molecular forces derived from the field-free potentials may be more important than previously assessed.

In the present work, the wave packet dynamics of the

---

photodissociation of $H_2^+$ under excitation by laser pulses of short durations at 329.7 nm are studied. The detailed mechanism for the formation of structured fragment kinetic energy spectra is examined by following the evolution of the coupled-channel wave functions in momentum space. Structures appear in the channel's momentum wave functions at $P \neq 0$, as the $v=0$ ground vibrational state is promoted to the repulsive channel then accelerated. The variations of these structures reflect the interplay between local laser-induced transitions and the accelerating–decelerating action of the field-free potentials, i.e., of intrinsic molecular forces. In this work, the wave packet dynamics are studied for two types of pulses of varying durations and peak intensities. In addition, two forms of channel couplings were considered. In the infinite-channel scheme limit and for a cw field, these two forms correspond to two different choices of the gauge: the so-called electric-field (EF) gauge, in which the matter–field interaction is of the length form, $\mu \cdot E$, and the radiation-field (RF) gauge, in which it is of the velocity form, $A \cdot p$.[26,27] In the present context, the system is modeled by a two-channel scheme and the radically different behaviors of the two coupling types with respect to the internuclear distance $R$ allows local intensity effects to be delineated.

Wave packets propagating on the two coupled channels of $H_2^+$ are generated by using a procedure which generalizes the construction of adiabatic time-dependent electronic states as proposed in previous work.[28–30] These time-dependent basis states were obtained by solving the local electronic time-dependent two-state Schrödinger equation in a formally exact manner using an effective pulse area and a geometrical phase related to the Berry phase associated with this adiabatic but exact evolution.[31] In the case of a periodic, i.e., a cw field, the Floquet solution of the local two-state time-evolution problem amounts to the local diagonalization of the diabatic Floquet or dressed-molecule Hamiltonian. Hence, in the time-dependent description, the introduction of the time-dependent electronic adiabatic basis states as particular solutions to the local two-state problem is the counterpart of the construction of dressed adiabatic electronic-field states defined in previous time-independent studies of this system in the presence of a cw laser.[32] Nonadiabatic couplings arising from the dependence of the local electronic two-state systems on the nuclear coordinates are partially reduced by further subjecting the local electronic system to a time-dependent unitary transformation which depends on the laser pulse shape. The generalized methodology obtained by introducing this unitary transformation to partially cancel nonadiabatic couplings associated with strong $R$ dependence of the transition dipole moment is presented in Sec. II. Section III reports the full details of the computational procedure. The results of the calculations are presented in Sec. IV and are analyzed in Sec. V in terms of the competition between laser-driven transfer of local amplitudes among the two coupled channels and the intrinsic wave packet dynamics on the field-free molecular potential energy surfaces.
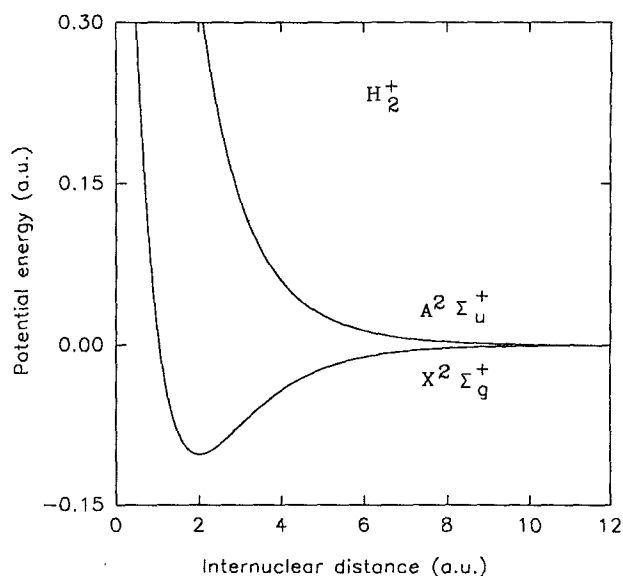


FIG. 1. Born-Openheimer potential energy surfaces $\epsilon_1(R)$ and $\epsilon_2(R)$ associated with the ground $X\,^2\Sigma_g$ and the excited $A\,^2\Sigma_u$ electronic states of $H_2^+$.

## II. METHODOLOGY

The time-dependent Schrödinger equation

$$i\hbar\,\partial_t \begin{pmatrix} \chi_1 \\ \chi_2 \end{pmatrix} = \begin{pmatrix} \hat{T}_N + \epsilon_1(R) & V_{12}(R,t) \\ V_{12}(R,t) & \hat{T}_N + \epsilon_2(R) \end{pmatrix} \begin{pmatrix} \chi_1 \\ \chi_2 \end{pmatrix} \qquad (1)$$

describes a two-channel molecular system driven by an external force field which gives rise to the time-dependent channel coupling potential $V_{12}(R,t)$. In Eq. (1), $R$ represents collectively the nuclear coordinates, $\hat{T}_N = (-\hbar^2/2\mu)\partial^2/\partial R^2$ denotes the nuclear kinetic energy operator, and $\mu$ is the reduced mass of the molecule. For the dissociation of $H_2^+$ under the influence of a laser pulse described by the electric-field vector $\mathbf{E}(t)$, $\epsilon_1(R)$ and $\epsilon_2(R)$ denote the Born–Oppenheimer (BO) potential energy surfaces of the $X\,^2\Sigma_g$ and $A\,^2\Sigma_u$ states, respectively (Fig. 1), and

$$V_{12}(R,t) = \mathbf{f}(R)\cdot\mathbf{E}(t), \qquad (2)$$

where, in the so-called electric-field (EF) or length gauge, $\mathbf{f}(R)$ is the $R$-dependent dipole moment $\mu_{12}(R)$ governing the transition between the two electronic states. In the radiation-field (RF) or velocity gauge, $\mathbf{f}(R)$ represents the $R$-dependent matrix element of the electronic momentum vector $\mathbf{p}$ linking the two electronic states mentioned above. The cw-field expression for $\mathbf{f}(R)$ in this gauge will be used in the calculations reported in the following sections even when the laser-field amplitude is modulated by a narrow Gaussian envelope. Thus

$$\mathbf{f}(R) = \begin{cases} \mu_{12}(R), & \text{in EF gauge} \\ \dfrac{\omega_{21}(R)}{\omega}\mu_{12}(R), & \text{in RF gauge,} \end{cases} \qquad (3)$$

where $\omega_{21}(R) \equiv (\epsilon_2 - \epsilon_1)/\hbar$ is the Bohr frequency for the local transition between the two electronic states and $\omega$ is the laser-field's carrier wave frequency.

Following the developments in Refs. 28–30, if $f(R)$ depends on $R$ weakly, then a local two-level picture can be obtained in the short-time limit by introducing the channel interaction-picture amplitudes defined by

$$\chi_k(R,t) = e^{-(i/\hbar)(\hat{T}_N + \epsilon_k)(t-t_0)}\chi_k^I(R,t), \quad k=1 \text{ or } 2 \quad (4)$$

up to error terms that are of second order in $\delta t \equiv (t - t_0)$. In this case, Eq. (1) implies

$$i\hbar \, \partial_t \begin{pmatrix} \chi_1^I \\ \chi_2^I \end{pmatrix} = \begin{pmatrix} 0 & V_{12}(R,t)e^{+i\omega_{12}(t-t_0)} \\ V_{12}(R,t)e^{-i\omega_{12}(t-t_0)} & 0 \end{pmatrix}$$

$$\times \begin{pmatrix} \chi_1^I \\ \chi_2^I \end{pmatrix} + O(\delta t^2). \quad (5)$$

This construction amounts to recognizing that, within the time scale set by the duration of an ultrashort laser pulse, laser-induced excitations tend to occur almost vertically, i.e., at nearly frozen nuclear positions. Formally, this is equivalent to introducing a new adiabatic electronic representation defined by the local (fixed $R$) two-state electronic Schrödinger equation. The error terms neglected in Eq. (5) are nonadiabatic couplings which result from the dependence of this new adiabatic electronic basis on the nuclear coordinates. These nonadiabatic couplings are of order $\delta t^2$ and are negligible on a sufficiently short time scale[28] which is estimated to be of the order of a few atomic units or a few tenth of a femtosecond. The remaining problem represented by Eq. (5) to wit the time evolution of an arbitrary laser-driven two-level system, has previously been solved in a formally exact manner.[31] The general nonperturbative, non-RWA (rotating-wave approximation) solution of Eq. (5) can be expressed as

$$\begin{pmatrix} \chi_1^I \\ \chi_2^I \end{pmatrix}_t = \begin{pmatrix} e^{-iF}\cos \mathscr{A}/2 & -e^{i[\omega_{12}(t-t_0)+\delta+F]}\sin \mathscr{A}/2 \\ e^{-i[\omega_{12}(t-t_0)+\delta+F]}\sin \mathscr{A}/2 & e^{iF}\cos \mathscr{A}/2 \end{pmatrix} \begin{pmatrix} \chi_1^I \\ \chi_2^I \end{pmatrix}_{t_0}, \quad (6)$$

where the effective pulse area $\mathscr{A}$ and phase angle $\delta$ are interrelated by

$$\mathscr{A}(R,t) \equiv \frac{2}{\hbar} \int_{t_0}^t dt' \, V_{12}(R,t')\sin \delta(R,t'), \quad (7a)$$

$$(\dot{\delta} + \omega_{12})\tan \mathscr{A} = \frac{2}{\hbar} V_{12} \cos \delta, \quad (7b)$$

and

$$F(R,t) = \frac{1}{\hbar} \int_{t_0}^t dt' \, V_{12} \cos \delta \, (1-\cos A)/\sin A. \quad (7c)$$

The above transformation of the two-channel coupled Eq. (1) to the equivalent local two-level Schrödinger Eq. (5) tacitly assumes that $V_{12}$ is slowly varying with respect to $R$. The calculations reported previously for the collisional Na–Ar system and the predissociative NaI molecule used this Condon approximation.[29,30] To investigate the dynamics of laser-driven ionic systems such as $H_2^+$ as a function of the gauge, i.e., of the interaction form within the same BO basis, it is important to take into account more accurately the variations of the couplings with respect to the nuclear coordinates. For this purpose, it is useful to introduce a single-parameter unitary transformation on the local two-state system, prior to the passage to the interaction picture, and write

$$\begin{pmatrix} \chi_1 \\ \chi_2 \end{pmatrix} = \begin{pmatrix} \cos \vartheta & i\sin \vartheta \\ i\sin \vartheta & \cos \vartheta \end{pmatrix} \begin{pmatrix} \tilde{\chi}_1 \\ \tilde{\chi}_2 \end{pmatrix} \equiv \mathbb{C}(\vartheta)\begin{pmatrix} \tilde{\chi}_1 \\ \tilde{\chi}_2 \end{pmatrix}. \quad (8)$$

The parameter $\vartheta$ depends on both $t$ and $R$. It will be chosen to ensure that the nonadiabatic coupling terms induced by $\mathbb{C}(\vartheta)$ cancel those associated with the $R$ dependence of $V_{12}$, up to order $\delta t^2$. More precisely, substitution of Eq. (8) into Eq. (1) gives

$$i\hbar \, \partial_t \begin{pmatrix} \tilde{\chi}_1 \\ \tilde{\chi}_2 \end{pmatrix} = \left\{ \begin{pmatrix} \hat{T}_N + \epsilon_1 \cos^2 \vartheta + \epsilon_2 \sin^2 \vartheta + \frac{\hbar^2}{2\mu}(\partial_R\vartheta)^2 & V_{12} + i\hbar \sin \vartheta \cos \vartheta \omega_{12} + \hbar\dot{\vartheta} \\ V_{12} - i\hbar \sin \vartheta \cos \vartheta \omega_{12} + \hbar\dot{\vartheta} & \hat{T}_N + \epsilon_2 \cos^2 \vartheta + \epsilon_1 \sin^2 \vartheta + \frac{\hbar^2}{2\mu}(\partial_R\vartheta)^2 \end{pmatrix} \right.$$

$$\left. + \frac{\hbar}{2\mu}[\partial_R\vartheta \hat{P}_R + \text{h.c.}]\begin{pmatrix} 0 & 1 \\ 1 & 0 \end{pmatrix} \right\} \begin{pmatrix} \tilde{\chi}_1 \\ \tilde{\chi}_2 \end{pmatrix}. \quad (9)$$

Since $\vartheta$ is anticipated to be of order $\delta t^1$, the above can be written as

$$ i\hbar\,\partial_t \begin{pmatrix} \widetilde{\chi}_1 \\ \widetilde{\chi}_2 \end{pmatrix} = \left\{ \begin{pmatrix} \hat{T}_N + \epsilon_1(R) & V_{12} + i\hbar\vartheta\omega_{12} + \hbar\dot{\vartheta} \\ V_{12} - i\hbar\vartheta\omega_{12} + \hbar\dot{\vartheta} & \hat{T}_N + \epsilon_2(R) \end{pmatrix} + \frac{\hbar}{2\mu}[\partial_R\vartheta\hat{P}_R + \text{h.c.}]\begin{pmatrix} 0 & 1 \\ 1 & 0 \end{pmatrix} + O(\delta t^2) \right\} \begin{pmatrix} \widetilde{\chi}_1 \\ \widetilde{\chi}_2 \end{pmatrix}. \tag{10} $$

By switching to the interaction picture using the Dirac transformation,

$$ \widetilde{\chi}_k(R,t) = e^{-(i/\hbar)(\hat{T}_N+\epsilon_k)(t-t_0)}\widetilde{\chi}_k^I(R,t), \quad k=1 \text{ or } 2, \tag{11} $$

Eq. (10) gives

$$ i\hbar\,\partial_t \begin{pmatrix} \widetilde{\chi}_1^I \\ \widetilde{\chi}_2^I \end{pmatrix} = \left\{ \begin{pmatrix} 0 & \left\{V_{12} + i\hbar\vartheta\omega_{12} + \hbar\dot{\vartheta} + \frac{(t-t_0)}{2\mu}[\partial_R(V_{12}+\hbar\dot{\vartheta})\hat{P}_R + \text{h.c.}]\right\}e^{+i\omega_{12}(t-t_0)} \\ \left\{V_{12} - i\hbar\vartheta\omega_{12} + \hbar\dot{\vartheta} + \frac{(t-t_0)}{2\mu}[\partial_R(V_{12}+\hbar\dot{\vartheta})\hat{P}_R + \text{h.c.}]\right\}e^{-i\omega_{12}(t-t_0)} & 0 \end{pmatrix} + \frac{\hbar}{2\mu}[\partial_R\vartheta\hat{P}_R + \text{h.c.}]\begin{pmatrix} 0 & 1 \\ 1 & 0 \end{pmatrix} \right\} $$

$$ \times \begin{pmatrix} \widetilde{\chi}_1 \\ \widetilde{\chi}_2 \end{pmatrix} + O(\delta t^2), \tag{12} $$

where use has been made of the result ($k=1$ or $2$)

$$ e^{(i/\hbar)(\hat{T}_N+\epsilon_k)(t-t_0)}[V_{12} - (-)^k i\hbar\vartheta\omega_{12} + \hbar\dot{\vartheta}]e^{-(i/\hbar)(\hat{T}_N+\epsilon_k)(t-t_0)} $$

$$ = V_{12} - (-)^k i\hbar\vartheta\omega_{12} + \hbar\dot{\vartheta} + \frac{(t-t_0)}{2\mu}[\partial_R(V_{12}+\hbar\dot{\vartheta})\hat{P}_R + \text{h.c.}] + O(\delta t^2). \tag{13} $$

Equation (13) is obtained by expanding the exponentials on the left side in Taylor series. The nonadiabatic coupling terms on the right arise from the $R$ dependence of the field-induced coupling $V_{12}$. They are canceled by selecting $\vartheta$ to be a solution to the following $R$-parameterized differential equation with respect to $t$

$$ (t-t_0)\dot{\vartheta} + \vartheta = -(t-t_0)V_{12}(R,t)/\hbar, \tag{14} $$

with initial condition $\vartheta(R,t_0)=0$, at all $R$, denoting the identity transformation at $t=t_0$. This gives

$$ \vartheta(R,t) = -\int_{t_0}^{t} dt' V_{12}(R,t')(t'-t_0)/\hbar(t-t_0). \tag{15} $$

With this choice, Eq. (12) reduces to a local two-level Schrödinger equation

$$ i\hbar\,\partial_t \begin{pmatrix} \widetilde{\chi}_1^I \\ \widetilde{\chi}_2^I \end{pmatrix} = \begin{pmatrix} 0 & \overline{V}_{12}(R,t) \\ \overline{V}_{12}(R,t) & 0 \end{pmatrix} \begin{pmatrix} \widetilde{\chi}_1^I \\ \widetilde{\chi}_2^I \end{pmatrix} + O(\delta t^2), \tag{16} $$

with

$$ \overline{V}_{12}(R,t) \equiv \frac{\int_{t_0}^{t} dt' V_{12}(R,t')(t'-t_0)}{(t-t_0)^2} = -\frac{\hbar\vartheta(R,t)}{(t-t_0)}, \tag{17} $$

defining an effective channel coupling. Note that in Eq. (16), this effective coupling is not accompanied by the dynamical phase $\exp(i\omega_{12}t)$ as in Eq. (5). Thus, Eq. (16) denotes a local system of two degenerate levels coupled by the interaction $V_{12}$ which can be solved by the effective area method outlined in Eqs. (6) and (7). For a degenerate two-level system, Eq. (7b) is satisfied by

$$ \delta = \pi/2, \tag{18a} $$

$F=0$ and the expression for the effective area simplifies to

$$ \mathscr{A}(R,t) = \frac{2}{\hbar}\int_{t_0}^{t} dt' \overline{V}_{12}(r,t'). \tag{18b} $$

Hence, the transformation $\mathscr{C}(\vartheta)$ has facilitated considerably the numerical task in addition to correctly accounting for the variation of the original channel coupling $V_{12}$ with $R$. Gathering Eqs. (8), (11), and (6) with $\mathscr{A}$ and $\delta$ given by Eqs. (18), the final expression for the solutions of Eq. (1) for short times is obtained

$$ \begin{pmatrix} \chi_1 \\ \chi_2 \end{pmatrix}_t \cong \begin{pmatrix} \cos\vartheta & i\sin\vartheta \\ i\sin\vartheta & \cos\vartheta \end{pmatrix} \begin{pmatrix} e^{-(i/\hbar)(\hat{T}_N+\epsilon_1)(t-t_0)} & 0 \\ 0 & e^{-(i/\hbar)(\hat{T}_N+\epsilon_2)(t-t_0)} \end{pmatrix} \begin{pmatrix} \cos\frac{\mathscr{A}}{2} & -i\sin\frac{\mathscr{A}}{2} \\ -i\sin\frac{\mathscr{A}}{2} & \cos\frac{\mathscr{A}}{2} \end{pmatrix} \begin{pmatrix} \chi_1 \\ \chi_2 \end{pmatrix}_{t_0} $$

$$ \cong e^{i\vartheta\begin{pmatrix} 0 & 1 \\ 1 & 0 \end{pmatrix}} \begin{pmatrix} e^{-(i/\hbar)(\hat{T}_N+\epsilon_1)(t-t_0)} & 0 \\ 0 & e^{-(i/\hbar)(\hat{T}_N+\epsilon_2)(t-t_0)} \end{pmatrix} e^{-i\frac{\mathscr{A}}{2}\begin{pmatrix} 0 & 1 \\ 1 & 0 \end{pmatrix}} \begin{pmatrix} \chi_1 \\ \chi_2 \end{pmatrix}_{t_0}. \tag{19} $$

Note that if the mean-value theorem is used to write the integrals in Eqs. (17) and (18b) in the form

$$\overline{V}_{12}(R,t) = -\frac{\hbar\vartheta(R,t)}{(t-t_0)} = \frac{1}{2} V_{12}(R,\bar{t}), \qquad (20a)$$

$$\mathscr{A}(R,t) = \frac{1}{\hbar} V_{12}(R,\bar{t})(t-t_0), \qquad (20b)$$

for a certain $\bar{t}\in[t_0,t]$, then Eq. (19) assumes the form of a third-order split-operator expression.[16,33] However, the present formulation offers two advantages over the well-known split-operator method. Conceptually, it demonstrates clearly the relation between the original two-channel time-dependent problem and the time evolution of an effective local two-level system, up to order $\delta t^2$. It provides a simple picture of the wave packet dynamics in which local excitations by the laser pulse are in competition with the acceleration or deceleration effects of the field-free potential energy surfaces on the excited wave packets. Moreover, while the split-operator formula requires the evaluation of $V_{12}$ at an appropriate $\bar{t}\in[t_0,t]$, which is usually confused with $t_0$ or $t$ in practical implementations, thereby introducing a further approximation, the construction of $\vartheta$ and $\mathscr{A}$ via Eqs. (17) and (18) removes this ambiguity. As an example, with $V_{12}$ given by Eq. (2) and $\mathbf{E}(t)$ of the form

$$\mathbf{E}(t) = \mathbf{E}_0 \cos \omega t, \qquad (21)$$

denoting a cw field, $\overline{V}_{12}$, $\vartheta$ and $\mathscr{A}$ can be expressed in closed forms as

$$\overline{V}_{12}(R,t) = -\frac{\hbar\vartheta(R,t)}{(t-t_0)}$$
$$= V_{12}^0(R)\left\{\frac{\sin \omega t}{\omega(t-t_0)} + \frac{\cos \omega t - \cos \omega t_0}{\omega^2(t-t_0)^2}\right\}, \qquad (22a)$$

$$\mathscr{A}(R,t) = \frac{2V_{12}^0(R)}{\hbar\omega}\left[\frac{\cos \omega t - \cos \omega t_0}{\omega(t-t_0)}\right], \qquad (22b)$$

where

$$V_{12}^0(R) \equiv \mathbf{f}(R)\cdot\mathbf{E}_0$$

is independent of time. For pulsed lasers, the field amplitude $E_0$ is modulated in time so that $\overline{V}_{12}$, $\vartheta$, and $\mathscr{A}$ must be calculated by numerical integrations as is done in the applications reported in the following sections.

## III. COMPUTATIONAL DETAILS

### A. Potential and couplings

The dissociation of H$_2^+$ in the presence of a laser pulse can be viewed as a two-state process

$$\text{H}_2^+(X\,^2\Sigma_g) \xrightarrow{\hbar\omega} \text{H}_2^+(A\,^2\Sigma_u) \to \text{H}(^2S) + \text{H}^+. \qquad (23)$$
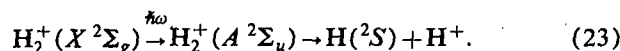
The BO potential energy surfaces $\epsilon_1$ and $\epsilon_2$ (Fig. 1), representing the two electronic states $X\,^2\Sigma_g$ and $A\,^2\Sigma_u$ are taken from Bunkin and Tugov,[34]

$$\epsilon_k(R) = D_0 \exp[-\alpha(R-R_e)]\{\exp[-\alpha(R-R_e)] - 2t_k\}, \qquad (24)$$

with

$$D_0 = 2.7925 \text{ eV}, \quad \alpha = 0.72 \text{ a.u.}, \quad R_e = 2.0 \text{ a.u.},$$
$$t_1 = 1.0, \quad t_2 = -1.11. \qquad (25)$$

The transition dipole moment between the two states

$$\mu_{12}(R) = \mu(R_e) + \frac{\mu'(R_e)}{\alpha y}\{1 - \exp[-\alpha y(R-R_e)]\}, \qquad (26a)$$

with

$$\mu(R_e) = 1.07 \text{ a.u.}, \quad \mu'(R_e) = 0.369 \text{ a.u.}, \quad y = -0.055, \qquad (26b)$$

also taken from this reference, gives the channel coupling potentials in the EF and RF gauge according to Eqs. (2) and (3). The laser field is represented by a function of the form

$$\mathbf{E}(t) = \mathbf{E}_0(t)\cos \omega t. \qquad (27)$$

Two pulse shapes were considered corresponding to two different functional forms of the field envelope $\mathbf{E}_0(t)$. In the case of a rectangular pulse,

$$\mathbf{E}_0(t) = \begin{cases} \mathbf{E}_0^M, & 0 < t < t_f \\ 0, & \text{otherwise}, \end{cases} \qquad (28)$$

and $t_f$ defines the pulse duration. In the case of a Gaussian pulse

$$\mathbf{E}_0(t) = \mathbf{E}_0^M \exp\{-\ln 2(\gamma/t_c)^2(t-t_c)^2\} \qquad (29)$$

denotes a pulse centered at $t_c$ with a full width at half maximum (FWHM) equal to $2t_c/\gamma$. With $\gamma = 5/2$, the values of $\mathbf{E}_0$ at $t=0$ and $t=2t_c$ are a hundred times smaller than the peak value $\mathbf{E}_0^M$. The calculations reported below use this definition of the Gaussian pulse. In addition, the field was considered switched on at $t=0$ and completely switched off at $2t_c$, so that the total width of the Gaussian pulse is identified with $2t_c$.

For both types of pulses, the peak intensity of the laser field is given in terms of $\mathbf{E}_0^M$ by

$$|\mathbf{E}_0^M| \text{ (a.u.)} \times 2.195 \times 10^5 (\text{cm}^{-1}/\text{a.u.})$$
$$= 1.17 \times 10^{-3}[I^M(\text{W/cm}^2)]^{1/2}, \qquad (30)$$

and the carrier-wave frequency $\omega$ corresponds to a wavelength of 329.7 nm. At this wavelength, the field is resonant with the Bohr frequency at $R = R_x = 3.6$ a.u. At $R = R_e$, the field is resonant only for a three-photon process.

### B. Initial wave packet and wave packet analysis

Neglecting rotational motions which are expected to have significant effects only at times longer than the duration of the subpicosecond pulses considered here,[17,24] the coupled wave packet algorithm represented by Eq. (19) was used in generating the time-dependent radial wave functions associated with the two coupled molecular chan-

nels of $H_2^+$. The initial condition corresponds to the $v=0$ vibrational state $\phi_0(R)$ of the ground-state manifold. Thus,

$$\chi_1(R,0) = \phi_0(R),$$

$$\chi_2(R,0) = 0. \quad (31)$$

The wave packets $\chi_1$ and $\chi_2$ generated at time $t$ are used to calculate the channel populations $P_1$ and $P_2$

$$P_i(t) = \int_0^\infty dR \, |\chi_i(R,t)|^2, \quad i=1,2, \quad (32)$$

and average positions $\langle R \rangle_1$ and $\langle R \rangle_2$

$$\langle R \rangle_i(t) = \int_0^\infty dR \, |\chi_i(R,t)|^2 R/P_i(t)^{\tau}, \quad i=1,2. \quad (33)$$

The momentum-representation amplitudes $\tilde{\chi}_1(P,t)$ and $\tilde{\chi}_2(P,t)$ are also monitored as functions of time; their evolutions show the mechanism by which the structured kinetic energy spectra of the fragments are formed in complete dynamical details. Structures in the asymptotic momentum spectra will be identified in terms of a number $n$ of photons by

$$\frac{\hat{P}^2}{2\mu} + |E_{v=0}^{(0)}| = n\hbar\omega, \quad (34)$$

where $E_{v=0}^{(0)}$ is the energy of the initial $v=0$ vibrational state supported by the ground-state manifold.

## C. Algorithm

The numerical implementation of Eq. (19) requires the duration of the laser pulse to be divided into time slices $[t_i, t_{i+1}]$ of equal extension, $t_k \equiv k\delta t$, $k \in \mathbb{N}$. The calculations within each slice comprise three steps: firstly, the solution to the local two-level problem, Eq. (16), using the area $\mathscr{A}$, are constructed from amplitudes which were previously obtained at $t_i$. Secondly, the resulting interaction-picture wave functions are then propagated in an uncoupled manner on the field-free potential energy surfaces, and finally, the operation of the matrix $\mathbf{C}(\vartheta)$ gives the final amplitudes at the end of the time slice. Within each slice, the calculation of the effective coupling $\bar{V}_{12}$, the area $\mathscr{A}$, and the rotation angle $\vartheta$ requires only two time integrals to be evaluated once, since with $V_{12}$ in the separable form of Eq. (2), Eqs. (17) and (18b) also become separable

$$-\frac{\hbar\vartheta(R,t)}{(t-t_0)} = \bar{V}_{12}(R,t)$$

$$\equiv \mathbf{f}(R) \cdot \frac{\int_{t_0}^t dt' \mathbf{E}(t')(t'-t_0)}{(t-t_0)^2}$$

$$= \mathbf{f}(R) \cdot \mathbf{I}_1(t), \quad (35)$$

$$\mathscr{A}(R,t) = \frac{2}{\hbar} \mathbf{f}(R) \cdot \int_{t_0}^t d\tau \frac{\int_{t_0}^\tau dt' E(t')(t'-t_0)}{(\tau-t_0)^2}$$

$$= \frac{2}{\hbar} \mathbf{f}(R) \cdot \mathbf{I}_2(t). \quad (36)$$

TABLE I. Parameters used in the implementation of the adiabatic wave packet propagation algorithm.

| Parameter description | Value |
|---|---|
| Width $\delta t$ of time slices | 2.0 a.u. |
| Number of integration points: | |
| $n_1$ | 100 |
| $n_2$ | 10 |
| Parameters used in the implementation of the FFT split-operator formula: | |
| $N_{pos}$ | 2048 or 4096 |
| $\delta R$ | 0.02 a.u. |
| $\delta k$ | 0.153 or 0.0766 (a.u.) |

The integrals $\mathbf{I}_1(t)$ and $\mathbf{I}_2(t)$ defined above are related by

$$\mathbf{I}_2(t) = \int_{t_0}^t d\tau \, \mathbf{I}_1(\tau).$$

Thus, the numerical calculation of $\mathbf{I}_2$ at the end of a given time slice requires that $\mathbf{I}_1$ be calculated at each point of a uniform grid consisting of $n_1$ steps within the time slice. The calculation of $\mathbf{I}_1$, which involves an integral of $\mathbf{E}(t)$, in turn requires a finer grid defined by dividing each step of the first grid into $n_2$ subintervals. The various integrals are evaluated on the appropriate grids using an extended trapezoidal rule.[35] The integrals $\mathbf{I}_1$ and $\mathbf{I}_2$ obtained at the end point $t_i$ of the current time slice are subsequently multiplied by the local value of $\mathbf{f}(R)$ according to Eqs. (35) and (36) to give the value of $\mathscr{A}$ and $\vartheta$ at the discrete points of a spatial grid used in the fast-Fourier-transform algorithm (FFT) representation of the field-free propagators which, in turn, are expressed in the split-operator form

$$e^{-(i/\hbar)(\hat{T}_N+\epsilon_k)(t-t_0)} = e^{-(i/\hbar)\epsilon_k(t-t_0)/2} e^{-(i/\hbar)\hat{T}_N(t-t_0)}$$

$$\times e^{-(i/\hbar)\epsilon_k(t-t_0)/2} + O(\delta t^3). \quad (37)$$

The FFT algorithm[35] is used to go from the coordinate representation, in which the potential terms in Eq. (37) are diagonal, to the momentum representation, in which the central kinetic factor in Eq. (37) is diagonal. The same FFT algorithm is used to generate momentum-space wave functions from the wave packets in coordinate representation. This FFT algorithm employs direct and reciprocal grids with fixed step size $\delta R$ and $\delta k$, respectively, but of variable extensions. In the early stages of the dynamics, when the wave packets are still localized in the bound region, a relatively small grid is appropriate, whereas at later stages, as the wave packets are moving toward the asymptotic dissociation region and simultaneously undergo considerable spreadings, a large grid is required. An option for extending the grid size upon a restart run has been included in the numerical code. In addition to listing the values of the various parameters defined above, Table I gives two values of $N_{pos}$, the number of points in the spatial and momentum grids: the smaller spatial grid was found to be sufficient to represent the wave packets within the duration of the shorter pulses, i.e., for time $t \lesssim 20$ fs. The
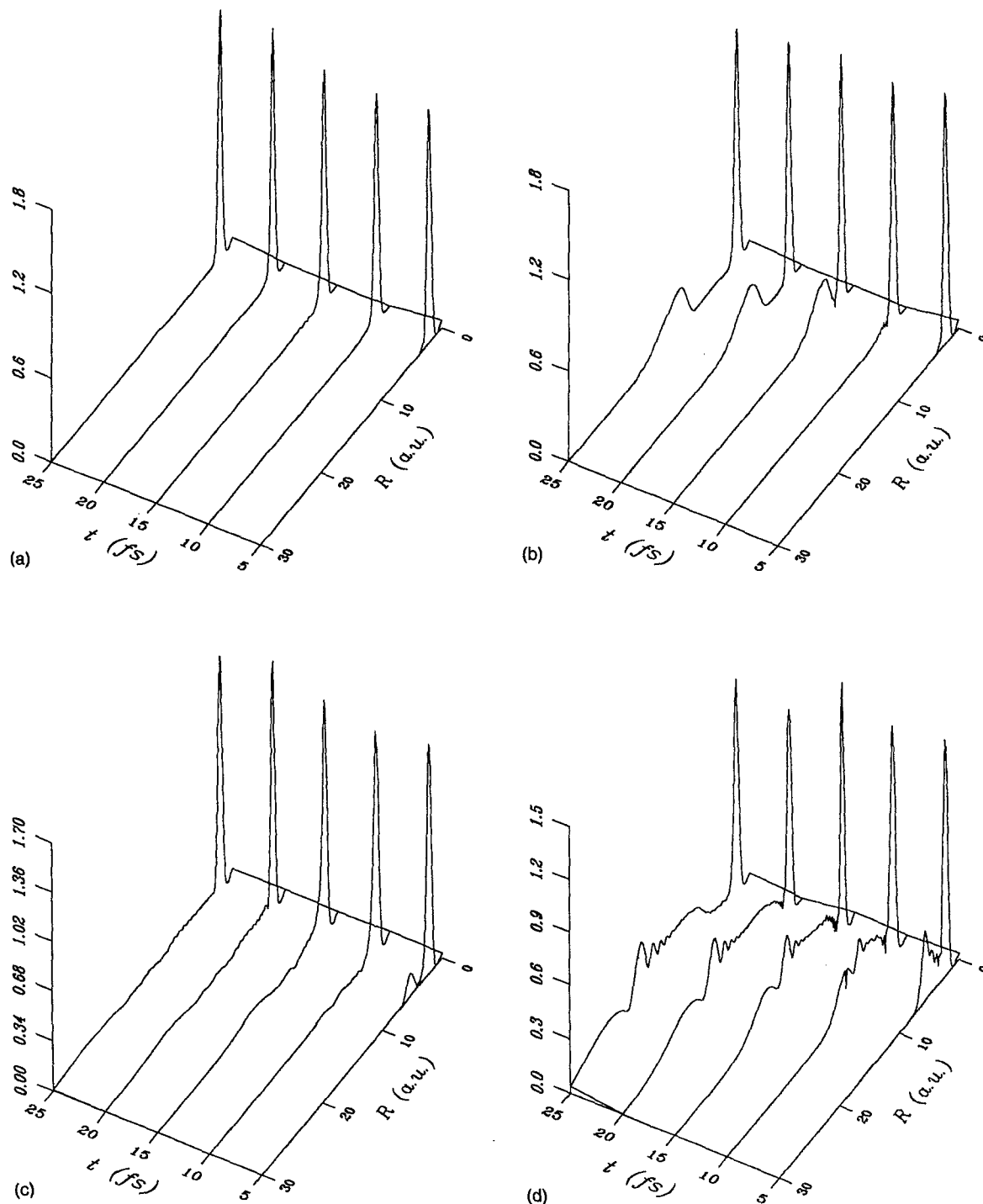
FIG. 2. Time evolution of the ground-state nuclear amplitudes $|\chi_1(R,t)|$ in the coordinate representation, within the duration of a 20 fs laser pulse delivering a peak intensity $I = 3.5 \times 10^{14}$ W/cm$^2$ and (a) of Gaussian shape in the EF gauge, (b) of Gaussian shape in the RF gauge, (c) of rectangular shape in the EF gauge, (d) of rectangular shape in the RF gauge.

larger grid was needed at longer time and in subsequent propagation of all unbound components of the wave packets toward the asymptotic dissociative region when the field has been switched off. This is systematically done in all cases and a stabilization of the channels' momentum-space wave functions with respect to further propagation indicates that this dissociative asymptotic limit has been reached. The spatial grid used in the FFT algorithm is also

employed in the numerical evaluations of the integrals in Eqs. (32) and (33).

## IV. RESULTS

Pulse durations of 5, 20, and 50 fs have been considered at peak intensities $I^M = I/4$ with $I$ ranging from $10^{12}$ to $3.5 \times 10^{14}$ W/cm$^2$. The following report gives the de-
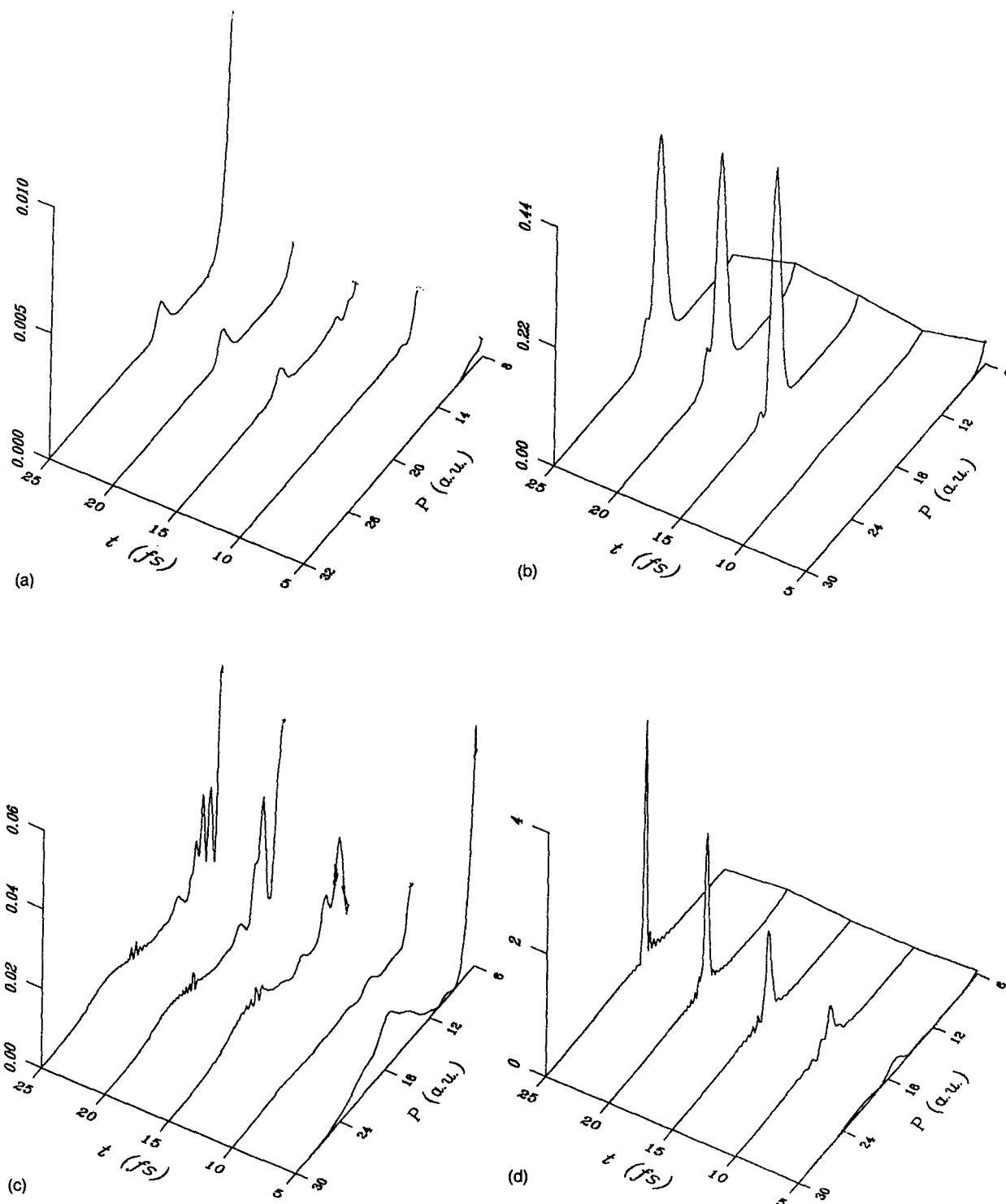
FIG. 3. Time evolution of the ground-state nuclear amplitudes $|\tilde{\chi}_1(P,t)|^2$ in the momentum representation, within the duration of a 20 fs laser pulse delivering a peak intensity $I=3.5\times10^{14}$ W/cm$^2$ and (a) of Gaussian shape in the EF gauge, (b) of Gaussian shape in the RF gauge, (c) of rectangular shape in the EF gauge, (d) of rectangular shape in the RF gauge.

tailed results for 20 fs pulses, as an illustration of the systematic analysis that has been made in all cases.

## A. 20 fs pulses

### 1. High intensity

Figures 2(a)–(d) shows the time evolution of the wave packets $\chi_1(R,t)$ in the coordinate representation for the

highest value of the field intensity considered, $I=3.5\times10^{14}$ W/cm$^2$. In the case of the RF gauge, for which a marked pulse-shape effect is observed, Figs. 2(b) and 2(d) indicate the existence of a strong dissociative component in the ground-state amplitude. In the EF gauge, Figs. 2(a) and 2(c), this amplitude remains much more localized in the
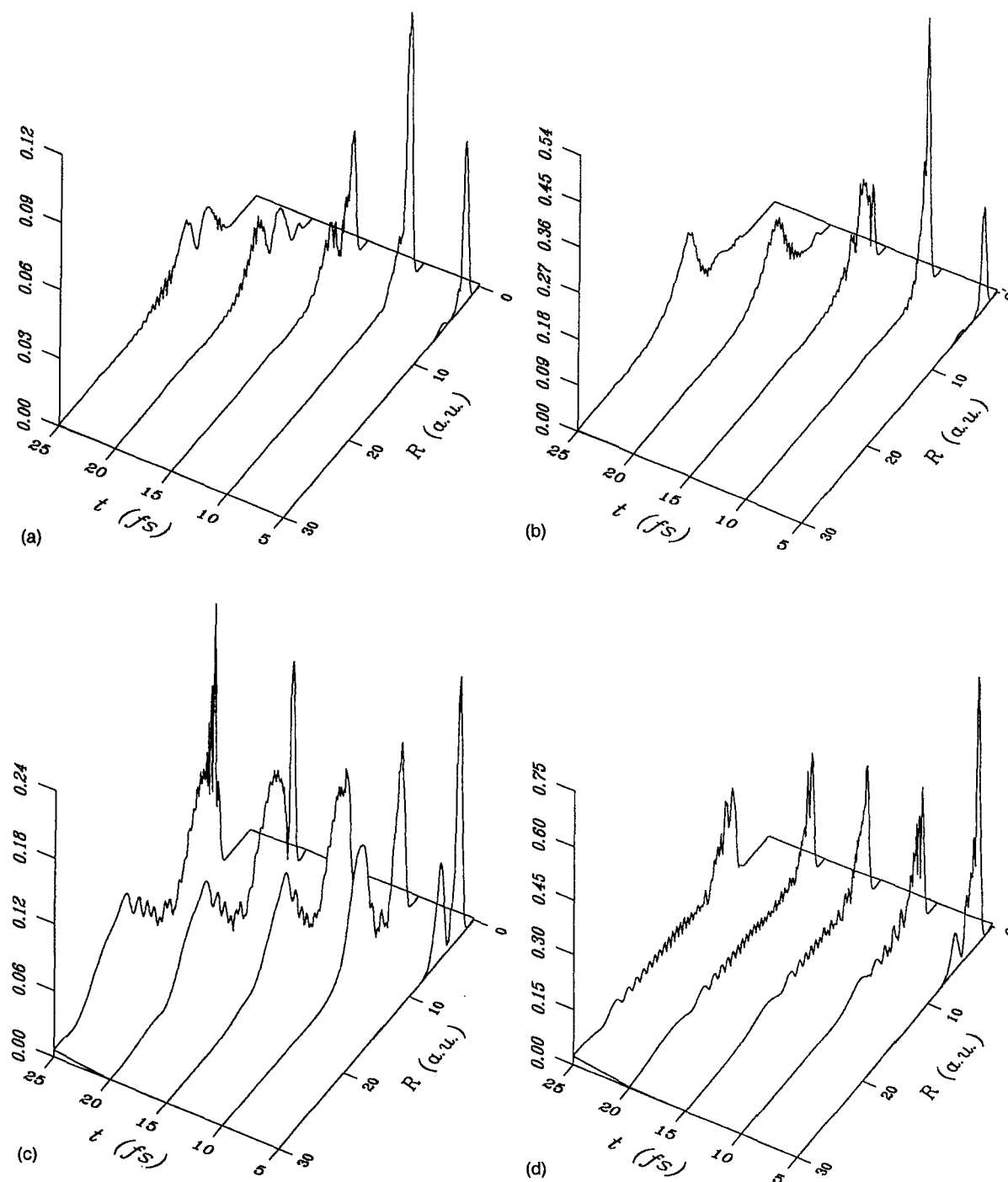
FIG. 4. Time evolution of the excited-state nuclear amplitudes $|\chi_2(R,t)|$ in the coordinate representation, within the duration of a 20 fs laser pulse delivering a peak intensity $I = 3.5 \times 10^{14}$ W/cm$^2$ and (a) of Gaussian shape in the EF gauge, (b) of Gaussian shape in the RF gauge, (c) of rectangular shape in the EF gauge, (d) of rectangular shape in the RF gauge.

bound region particularly in the case of a Gaussian pulse, Fig. 2(a). The replacement of the Gaussian pulse by the rectangular pulse, Fig. 2(c), produces only a slight change in the ground-state amplitude and a more prominent dissociative tail emerges at an early stage, $t = 5$ fs. The presence of a dissociative component in the ground-state amplitude $\chi_1$ is seen more clearly in the momentum representation. The momentum-space wave functions

$\tilde{\chi}_1(P,t)$ shown in Figs. 3(a)–3(d) correspond to those in coordinate representation shown in Figs. 2(a)–2(d). In all cases and at all times, $\tilde{\chi}_1(P,t)$ exhibits a broad peak centered at $P = 0.0$ a.u. which corresponds to the initial $v = 0$ vibrational wave packet and which, in the EF gauge, remains prominent at all times. This peak is only partially shown in Figs. 3(a) and 3(c) for the EF gauge, and it is not shown at all in Figs. 3(b) and 3(d) for the RF gauge.
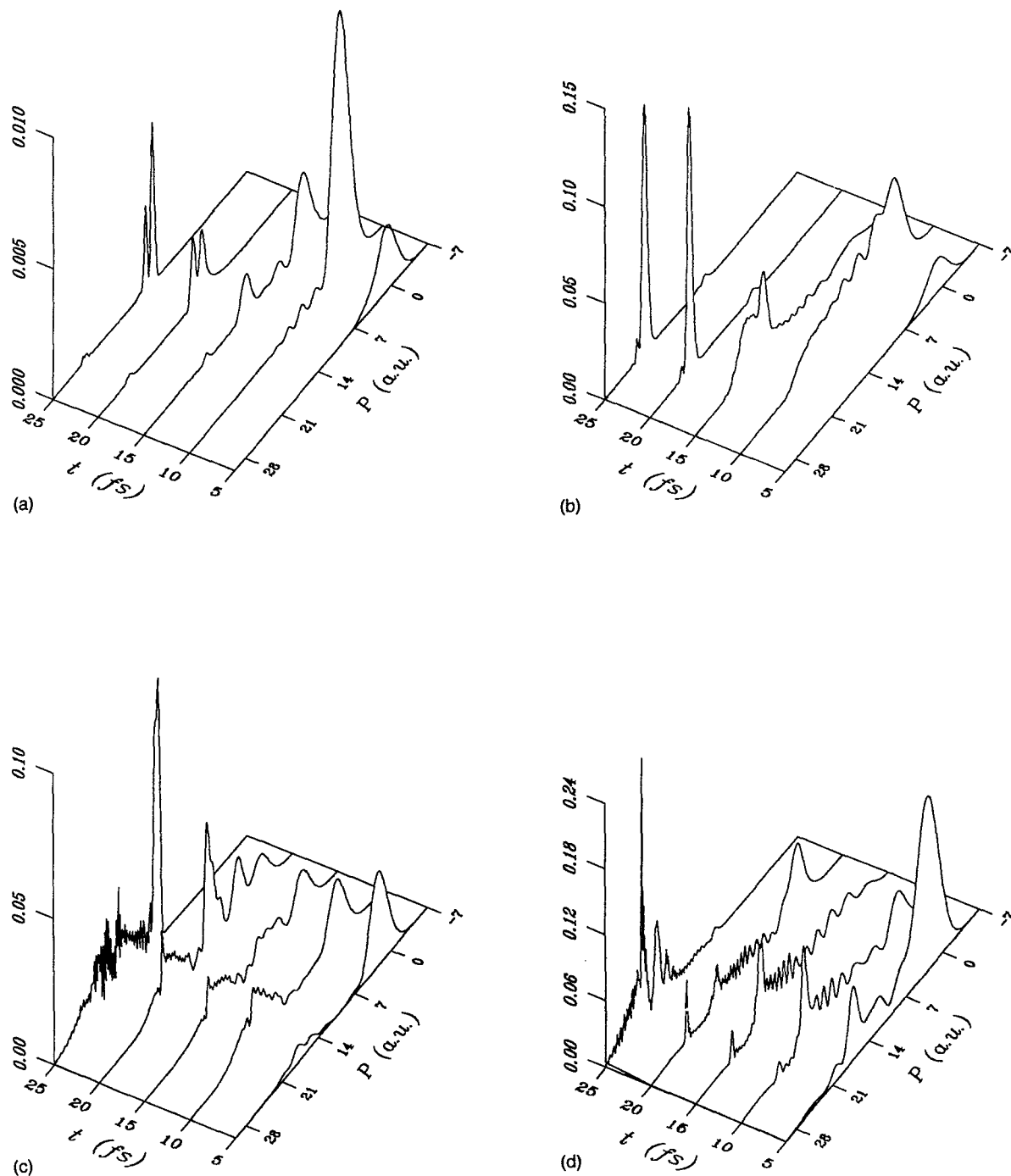
FIG. 5. Time evolution of the excited-state nuclear amplitudes $|\tilde{\chi}_2(P,t)|^2$ in the momentum representation, within the duration of a 20 fs laser pulse delivering a peak intensity $I=3.5\times10^{14}$ W/cm$^2$ and (a) of Gaussian shape in the EF gauge, (b) of Gaussian shape in the RF gauge, (c) of rectangular shape in the EF gauge, (d) of rectangular shape in the RF gauge.

In this gauge, as expected, the peak is very prominent at short times but gets depleted quickly in the course of the time evolution; at the end of the rectangular pulse, Fig. 3(d), this peak is dominated by the sharp peak at $P=18$ a.u. which, according to Eq. (34), would correspond to a fragmentation of the molecule in channel 1 after a net absorption of two photons. A broader and weaker two-photon structure is also observed in the ground-state momentum wave packet by the end of the Gaussian pulse, Fig. 3(a) for the EF gauge and Fig. 3(b) for the RF gauge. In Fig. 3(c), corresponding to the excitation by a rectangular pulse in the EF gauge, the dissociative component of $\tilde{\chi}_1(P,t)$ is also concentrated at this nominal two-photon position at $t=5$ fs. However it later evolves into a final
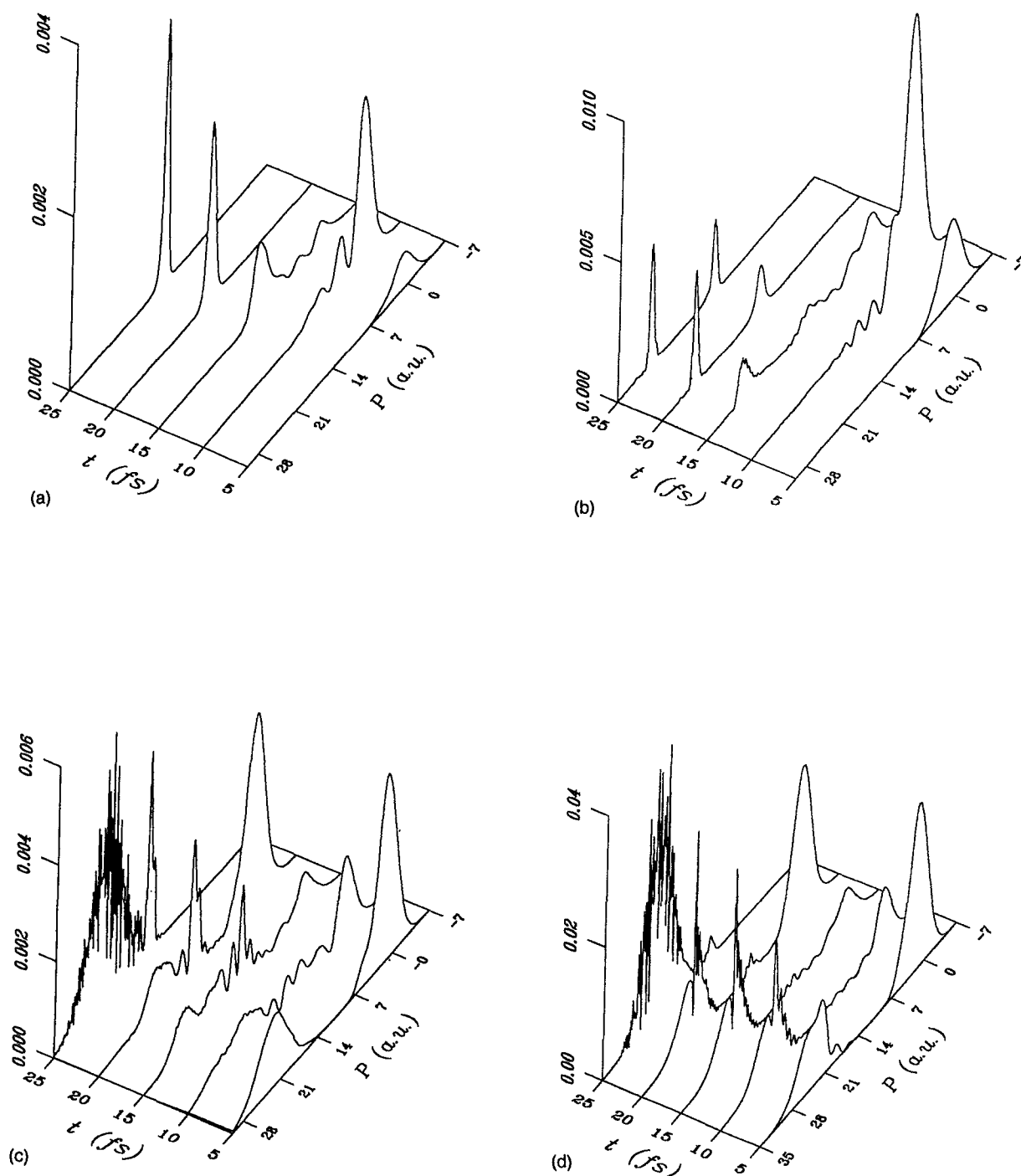
FIG. 6. Time evolution of the excited-state nuclear amplitudes $|\tilde{\chi}_2(P,t)|^2$ in the momentum representation, within the duration of a 20 fs laser pulse delivering a peak intensity $I=5.6\times10^{13}$ W/cm$^2$ and (a) of Gaussian shape in the EF gauge, (b) of Gaussian shape in the RF gauge, (c) of rectangular shape in the EF gauge, (d) of rectangular shape in the RF gauge.

structure which tends to concentrate at the one- and three-photon positions at $P=12$ and 24 a.u., respectively.

On the excited manifold, the time evolutions of the coordinate-space wave packets $\chi_2(R,t)$, Figs. 4(a)–4(d), reveal a stronger dependence of these amplitudes on pulse shape and gauge when compared to the ground-state am-

plitudes in Figs. 2(a)–2(d). The time evolutions of the corresponding momentum-space amplitudes $|\tilde{\chi}_2(P,t)|$ are shown in Figs. 5(a)–5(d). In all cases, the momentum-space wave packets initially (at $t=5$ fs) exhibit a prominent peak near $P=0$ reflecting the promotion of the initial-ground state $v=0$ vibrational wave packet to the upper
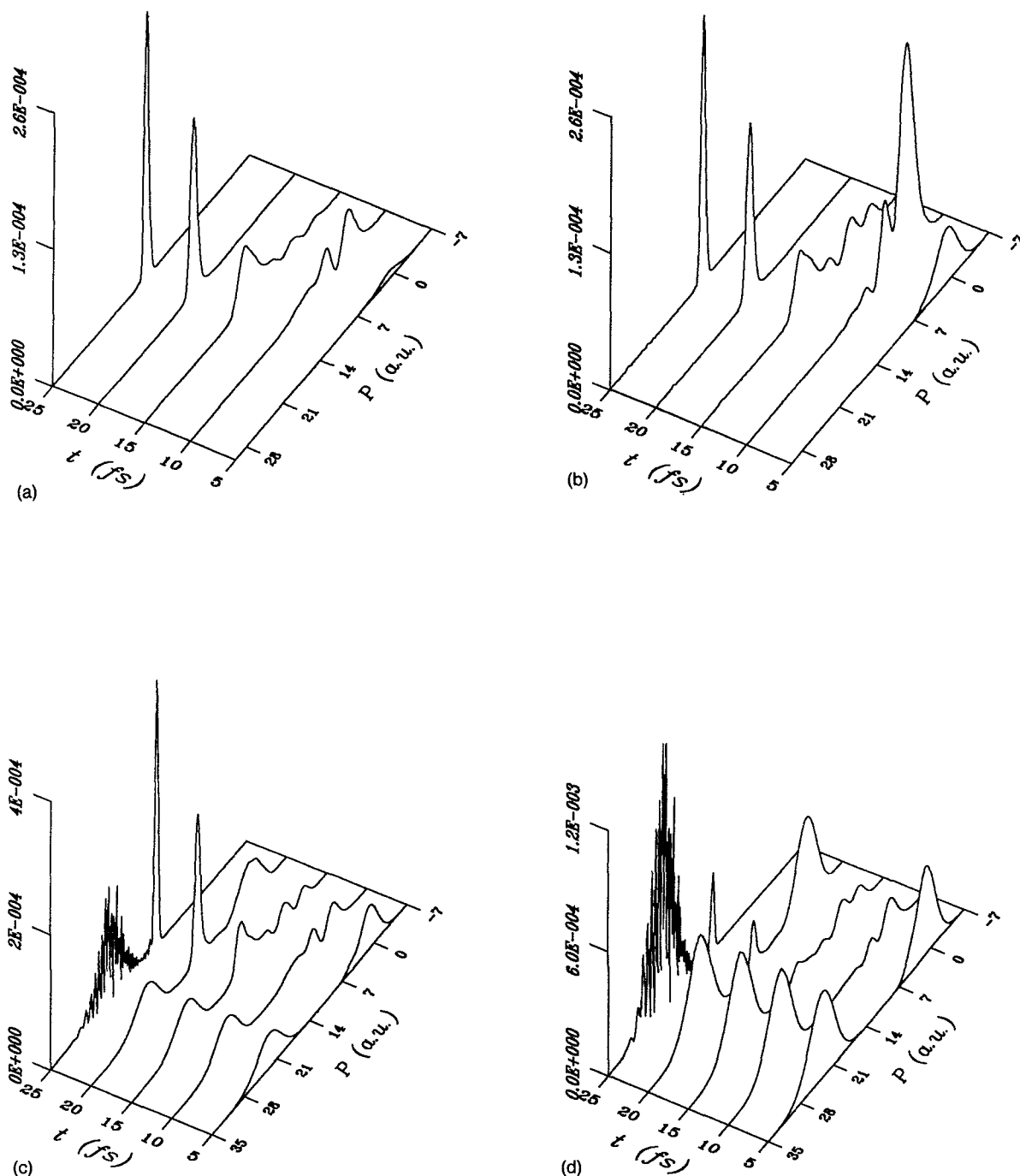
FIG. 7. Time evolution of the excited-state nuclear amplitudes $|\tilde{\chi}_2(P,t)|^2$ in the momentum representation, within the duration of a 20 fs laser pulse delivering a peak intensity $I = 10^{12}$ W/cm$^2$ and (a) of Gaussian shape in the EF gauge, (b) of Gaussian shape in the RF gauge, (c) of rectangular shape in the EF gauge, (d) of rectangular shape in the RF gauge.

surface. This promotion persists up to $t = 15$ fs., i.e., past the half-pulse width under a Gaussian pulse, Figs. 5(a) and 5(b), and until the end of the rectangular pulses of Figs. 5(c) and 5(d). Meanwhile, the previously promoted wave packet is accelerated to give a sharp structure at a final value of $P$ near 12 a.u. (the one-photon position) in the EF gauge, Figs. 5(a) and 5(c), and near 24 a.u. (the

three-photon position) in the RF gauge, Figs. 5(b) and 5(d). In the EF gauge, the excitation by a rectangular pulse also gives a relatively strong and broad beating structure encompassing the three-photon absorption region, Fig. 5(c). In contrast, the excitation by a Gaussian pulse, Fig. 5(a), only gives a very weak signal in this region. A weak signal is also found near the one-photon absorption

position in the final momentum distributions of Figs. 5(b) and 5(d) corresponding to a Gaussian and a rectangular pulse, respectively, treated in the RF gauge.

## 2. Lower intensities

For an intensity of $5.6 \times 10^{13}$ W/cm$^2$, the time-dependent momentum representation wave functions $\tilde{\chi}_2(P,t)$ are given in Figs. 6(a)–6(d). As in Figs. 5(c)–5(d), the rectangular pulses give rise to a broad beating structure in the nominal three-photon absorption region in both gauges, Figs. 6(c) and 6(d). In the case of the EF gauge, Fig. 6(c), this structure has gained intensity relative to the one-photon peak. In the RF gauge, Fig. 6(d), the one-photon signal in the final momentum distribution also becomes slightly stronger when compared to the situation at $I = 3.5 \times 10^{14}$ W/cm$^2$ in Fig. 5(d). The one-photon peak is still dominated by the three-photon broad structure. The final excited-state momentum distribution associated with a Gaussian pulse in the RF gauge, Fig. 6(b), exhibits two sharp peaks at the one- and three-photon positions. In comparison with the corresponding situation at higher intensity, Fig. 5(b), the one-photon signal has gained considerable amplitude relative to the three-photon peak. In contrast, in the EF gauge, Fig. 6(a), the excitation by a Gaussian pulse leads to a final momentum distribution on the upper channel which exhibits only a single sharp peak at the one-photon absorption position. On the ground-state manifold, the final momentum distribution for the Gaussian pulse in the EF gauge exhibits no noticeable structure beside the $P = 0$ a.u. peak associated with the initial $v = 0$ vibrational state. For the Gaussian pulse in the RF gauge, a small peak at the two-photon position, $P = 18$ a.u., emerges at $t = 15$ fs, i.e., at the same time as the three-photon structure appear in Fig. 6(b). A peak at the two-photon position also appears at an early stage of the time evolution of the ground state momentum-space wave function as the system is excited by a rectangular pulse irrespective of the gauge.

Figures 7(a)–7(d) shows the evolution of the excited-state wave packets in the momentum representation for an intensity of $I = 10^{12}$ W/cm$^2$. Figures 7(a) and 7(b) reveals that in both gauges excitation by a Gaussian pulse gives a final momentum distribution with a single sharp peak at the one-photon position. Figures 7(c) and 7(d) show that a rectangular pulse continues to give rise to a broad beating structure in the neighborhood of the three-photon absorption position along with a sharp peak at the one-photon position. In both gauges, this peak has gained considerable intensity to the expense of the three-photon structure.

Figure 8 shows the population $P_2(t)$ of the excited state as a function of time for the three intensities considered above. At the lower intensities, in both gauges, the excitation profile under a rectangular pulse exhibits a minimum at half the pulse width. For a rectangular pulse at $I = 3.5 \times 10^{14}$ W/cm$^2$, $P_2$ behaves in a more monotonic fashion. In the case of the RF gauge it falls from a value of 20% at $t = 5$ fs to a final plateau of about 7%, while in the EF gauge it rises slightly from $\sim 3.5\%$ at $t = 5$ fs to a final value of $\sim 5\%$. Note that the value of $P_2$ at $t = 5$ fs, denot-
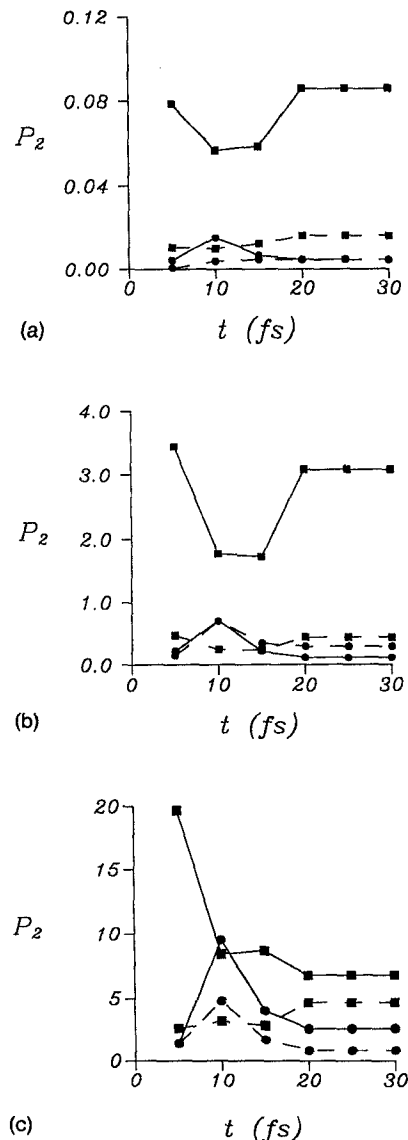


(a)

(b)

(c)

FIG. 8. Time evolution of the excitation probability $P_2(t)$ (in percents) obtained under the excitation by a rectangular pulse in the RF gauge (full lines with squares) or in the EF gauge (broken lines with squares) and by a Gaussian pulse in the RF gauge (full lines with circles) or in the EF gauge (broken lines with circles). The peak intensity of the pulse is $I = 10^{12}$ W/cm$^2$ in (a), $I = 5.6 \times 10^{13}$ W/cm$^2$ in (b), and $I = 3.5 \times 10^{14}$ W/cm$^2$ in (c).

ing a relatively early stage of the excitation by the rectangular pulses, behaves roughly as a linear function of $I$. For these rectangular pulses, $P_2$ exhibits oscillations at times earlier than 3.5 fs, making the investigation of its behavior with respect to the field intensity difficult. These oscillations may be due to transients arising from the sudden switching on of these pulses. In any event, on average, $P_2$ does exhibit a linear variation with $I$ at these early times. The excitation profiles associated with Gaussian pulses all exhibit a maximum at half the pulse width, when the peak intensity is delivered by the laser. For these pulses, the scale of the graphs shown in Fig. 8 does not allow a precise graphical estimate of the variation of $P_2(t \leqslant 5$ fs) with the peak intensity $I$. Table II gives the values of this transition

TABLE II. Short-time evolution of the excitation probability $P_2$ (in %) under Gaussian pulses of varying intensity in the EF and RF gauge.

| $P_2$ (%) $t$ (fs) | Gaussian pulse (EF gauge) | | | Gaussian pulse (RF gauge) | | |
|---|---|---|---|---|---|---|
| | $I=10^{12}$ (W/cm$^2$) | $I=5.6\times10^{13}$ (W/cm$^2$) | $I=3.5\times10^{14}$ (W/cm$^2$) | $I=10^{12}$ (W/cm$^2$) | $I=5.6\times10^{13}$ (W/cm$^2$) | $I=3.5\times10^{14}$ (W/cm$^2$) |
| 0.5 | $2.7\times10^{-6}$ | $1.5\times10^{-4}$ | $9.5\times10^{-4}$ | $1.9\times10^{-5}$ | $1.1\times10^{-3}$ | $6.9\times10^{-3}$ |
| 1.0 | $4.0\times10^{-6}$ | $2.2\times10^{-4}$ | $1.4\times10^{-3}$ | $3.4\times10^{-5}$ | $1.8\times10^{-3}$ | $1.1\times10^{-2}$ |
| 1.5 | $3.7\times10^{-6}$ | $2.1\times10^{-4}$ | $1.3\times10^{-3}$ | $3.4\times10^{-5}$ | $1.8\times10^{-3}$ | $1.0\times10^{-2}$ |
| 2.0 | $3.8\times10^{-6}$ | $2.2\times10^{-4}$ | $1.4\times10^{-3}$ | $3.0\times10^{-5}$ | $1.6\times10^{-2}$ | $1.0\times10^{-2}$ |
| 2.5 | $1.0\times10^{-5}$ | $6.0\times10^{-4}$ | $3.7\times10^{-3}$ | $8.3\times10^{-5}$ | $4.6\times10^{-3}$ | $2.8\times10^{-2}$ |
| 3.0 | $4.2\times10^{-5}$ | $2.3\times10^{-3}$ | $1.4\times10^{-2}$ | $3.3\times10^{-4}$ | $1.8\times10^{-2}$ | $1.1\times10^{-1}$ |
| 3.5 | $1.2\times10^{-4}$ | $6.9\times10^{-3}$ | $4.3\times10^{-2}$ | $9.5\times10^{-4}$ | $5.3\times10^{-2}$ | $3.2\times10^{-1}$ |
| 4.0 | $2.6\times10^{-4}$ | $1.4\times10^{-2}$ | $9.2\times10^{-2}$ | $2.0\times10^{-3}$ | $1.1\times10^{-1}$ | $6.8\times10^{-1}$ |
| 4.5 | $4.2\times10^{-4}$ | $2.3\times10^{-2}$ | $1.5\times10^{-1}$ | $3.2\times10^{-3}$ | $1.7\times10^{-1}$ | 1.1 |

probability obtained at short times under excitation by a Gaussian pulse in RF and EF gauges. The information in Table II shows once more that $P_2$ is a linear function of the field intensity at short times. From the results in Table II for Gaussian pulses and from the curves in Fig. 8 for the rectangular pulses, it is interesting to note that, at all $I$, the early excitation probability $P_2(t\leqslant5$ fs$)$ found in the RF gauge is ninefold larger than that found in the EF gauge. Since, in the early stage of the dynamics the wave packets are relatively well localized in the bound region where $\omega_{21}\sim3\omega$ which means that the RF gauge channel coupling, $V_{12}^{RF}$, is three times larger than its EF counterpart, $V_{12}^{EF}$, this observation is another indication of the linear scaling law $P_2\propto I^1$ obeyed by the excitation probability at short times.

The final momentum-space wave functions in Figs. 5–7 are evaluated at 25 fs, shortly after the pulse had been switched off. Although not asymptotic, these wave functions already exhibit the qualitative structures of the asymptotic momentum distributions on the upper channel. Similarly, the asymptotic ground-state momentum distributions are already reflected in the structure of $\widetilde{\chi}_1(P,t)$ at $t=25$ fs. The excited-state asymptotic momentum distributions arising from the irradiation of the system by 20 fs pulses of varying shape and intensity are gathered in Figs. 9(a)–9(c). The panels 9(a), 9(b), and 9(c) correspond to $I=10^{12}$, $5.6\times10^{13}$, and $3.5\times10^{14}$ W/cm$^2$, respectively. In each panel, the two spectra on the left are associated with a rectangular pulse, in the EF and RF gauge, and the two on the right are associated with a Gaussian pulse in the EF and RF gauge. The asymptotic ground-state momentum distributions are also already reflected in the structure of $\widetilde{\chi}_1(P,t)$ at $t=25$ fs.

### B. Pulse duration effects

The complete analysis of the coupled-wave packets evolution detailed previously for the excitation by 20 fs pulses have been repeated for two other pulse lengths. Using the same format as Figs. 9(a)–9(c), Figs. 10(a)–10(c), and Figs. 11(a)–11(c) show the asymptotic excited-state momentum distributions as a function of gauge, pulse shape, and peak intensity, for pulses of 50 and 5 fs, respectively. As seen by comparing Figs. 10(a)–10(c) with Figs. 9(a)–9(c), the longer pulses of 50 fs width produce qualitatively

the same spectra as their 20 fs counterparts. At the lowest intensity, Fig. 10(a), a net enhancement of the one-photon peak is noted in both gauges; the Gaussian pulse still leads to a single peak at $P=12$ a.u. while, in the case of the rectangular pulse, the broad beating structure in the three-photon region loses intensity at the benefit of the one-photon peak. In the RF gauge and for both pulse shapes, the peak at the one-photon position tends to disappear as the intensity is increased. In contrast, this peak remains the dominant feature in the spectra associated with the EF gauge, except for the case of a rectangular pulse at the intermediate intensity, $I=5.6\times10^{13}$ W/cm$^2$, Fig. 10(b), which gives rise to a rather strong broad beating structure in the three-photon region.

For the much shorter 5 fs pulses, Figs. 11(a)–11(c) shows asymptotic momentum spectra that are strikingly different from those in Figs. 9(a)–9(c) and 10(a)–10(c). An overall tendency for the three-photon pathway to be favored is observed in all cases, although a one-photon peak is still observed in the spectra associated with the Gaussian pulses. In the cases of the EF gauge, this peak survives the intensity increase from $10^{12}$ to $3.5\times10^{14}$ W/cm$^2$, whereas in the RF gauge, it is completely depleted at $I=3.5\times10^{14}$ W/cm$^2$.

## V. DISCUSSIONS

The presence of structures in the fragment kinetic energy spectra at positions corresponding to the absorption of integral number of photons, such as observed above through the asymptotic channel momentum distributions, has been rationalized elsewhere in terms of adiabatic or diabatic nuclear motion on the dressed-potential energy surfaces.[16,17,22–25] A three-photon absorption in the initial stage of the excitation has been proposed to give a seemingly natural explanation of the appearance of a peak at the three-photon nominal position in the spectra.[17,24] The results given in the previous section pertaining to the behavior of the transition probability at short times, $P_2(t\leqslant5$ fs$)\propto I$, indicate, rather, a one-photon nonresonant absorption in the early stage of the preparation of the excited-state wave packet.
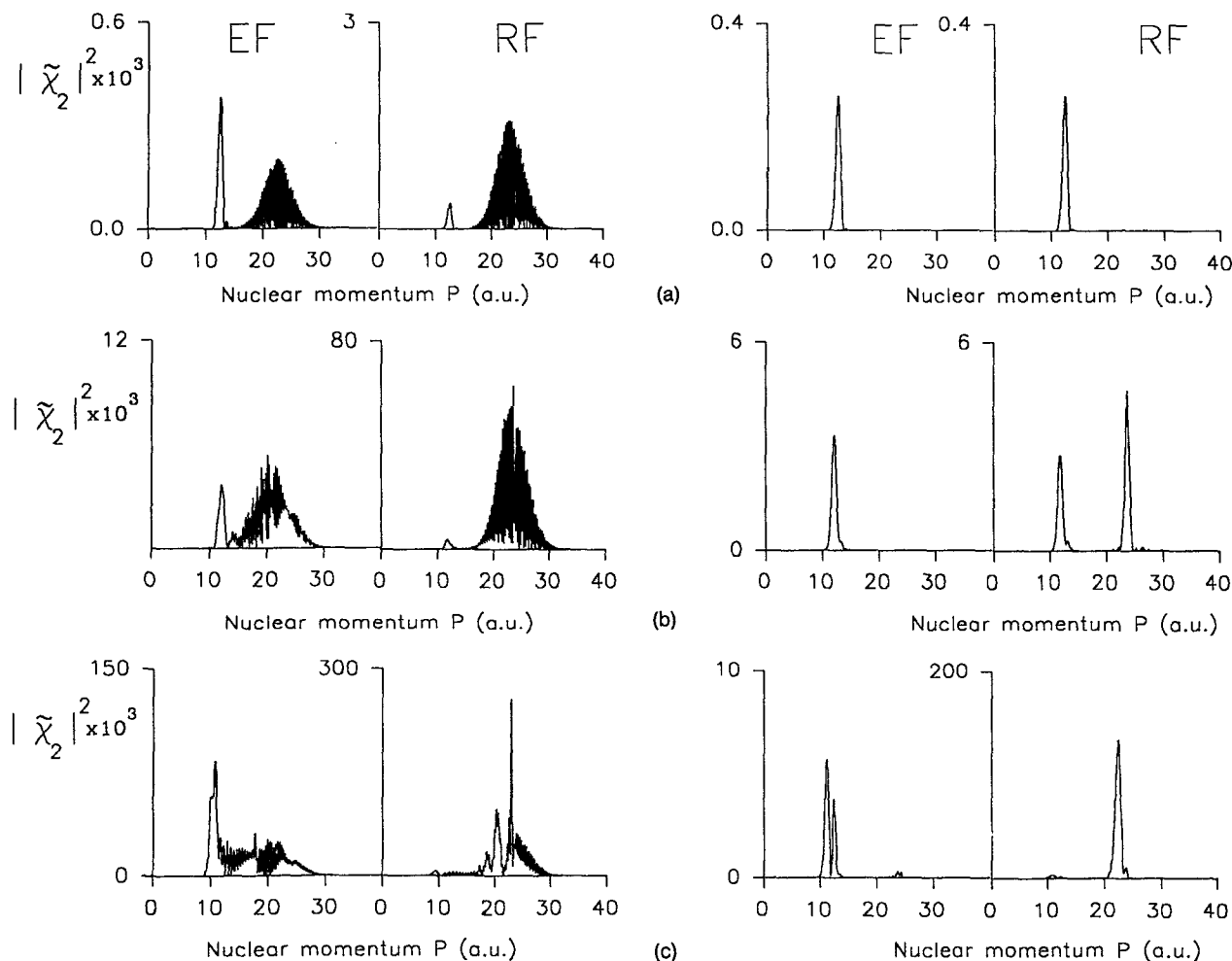
FIG. 9. Asymptotic momentum distributions $|\tilde{\chi}_2(P,\infty)|^2$ supported by the excited-state manifold, resulting from the excitation by a rectangular pulse (left panels) or a Gaussian pulse (right panels) of 20 fs duration and peak intensity (a) $I=10^{12}$ W/cm$^2$, (b) $I=5.6\times10^{13}$ W/cm$^2$, and (c) $I=3.5\times10^{14}$ W/cm$^2$. In each panel, the gauge employed is indicated explicitly.

Thus, a mechanism in which the initial preparation phase involves a three-photon absorption is improbable, particularly for the Gaussian pulses, since, at this early stage, corresponding to the rise of the pulse, the field intensity would be too weak to favor a third-order (three-photon) resonant process over a first-order (one-photon) nonresonant transition. The question then arises as to how a nominal three-photon peak can appear in the final kinetic energy spectra. Consider a wave packet instantly promoted from the ground $v=0$ state on the upper channel by a vertical transition at $R\sim R_e$: The promoted wave packet shares the same center ($R=R_e$), the same average momentum $P_0=0$ as the initial wave packet. Its instantaneous average energy is then $\langle E\rangle\sim E_{v=0}+3\hbar\omega$. If the field is switched off immediately after this excitation process, the excited wave packet would exit on this dissociative channel in field-free, i.e., conservative conditions. Therefore, it would be fully accelerated to gain a final kinetic energy equal to $\langle E\rangle$, i.e., at the so-called three-photon position, even though no real three-photon absorption has necessarily occured. In the cases presently under consideration, the pulses are not delta-function pulses, but act continuously

over a finite period of time, the pulse duration. During this time, the acceleration of the promoted wave packet is accompanied by the continuing action of the laser field which continuously pumps local population up to the excited-state channel and down to the ground-state manifold. At an early stage, the accelerated parts of the upper-channel wave packet are still localized in the bound region so that when they are transferred to the ground-state manifold, they feel an attractive potential, and may undergo a deceleration before being transferred back to the upper channel. This mechanism can give rise to a net acceleration of the upper channel wave packet to a final value which is much lower than the full acceleration to $P=24$ a.u. which would be gained under field-free conditions. For this mechanism to be operative, the rate for pumping local population up to the excited channel must be smaller than the rate with which the deceleration of a wave packet by the attractive ground potential occurs. Hence, a low field intensity will favor this mechanism. A one-photon peak in $\tilde{\chi}_2(P,t)$ is observed in the RF-gauge Gaussian pulse case only at low intensity, as seen in Figs. 9–11. For the longer rectangular pulses illustrated in Figs. 9 and 10, the RF-gauge asymp-
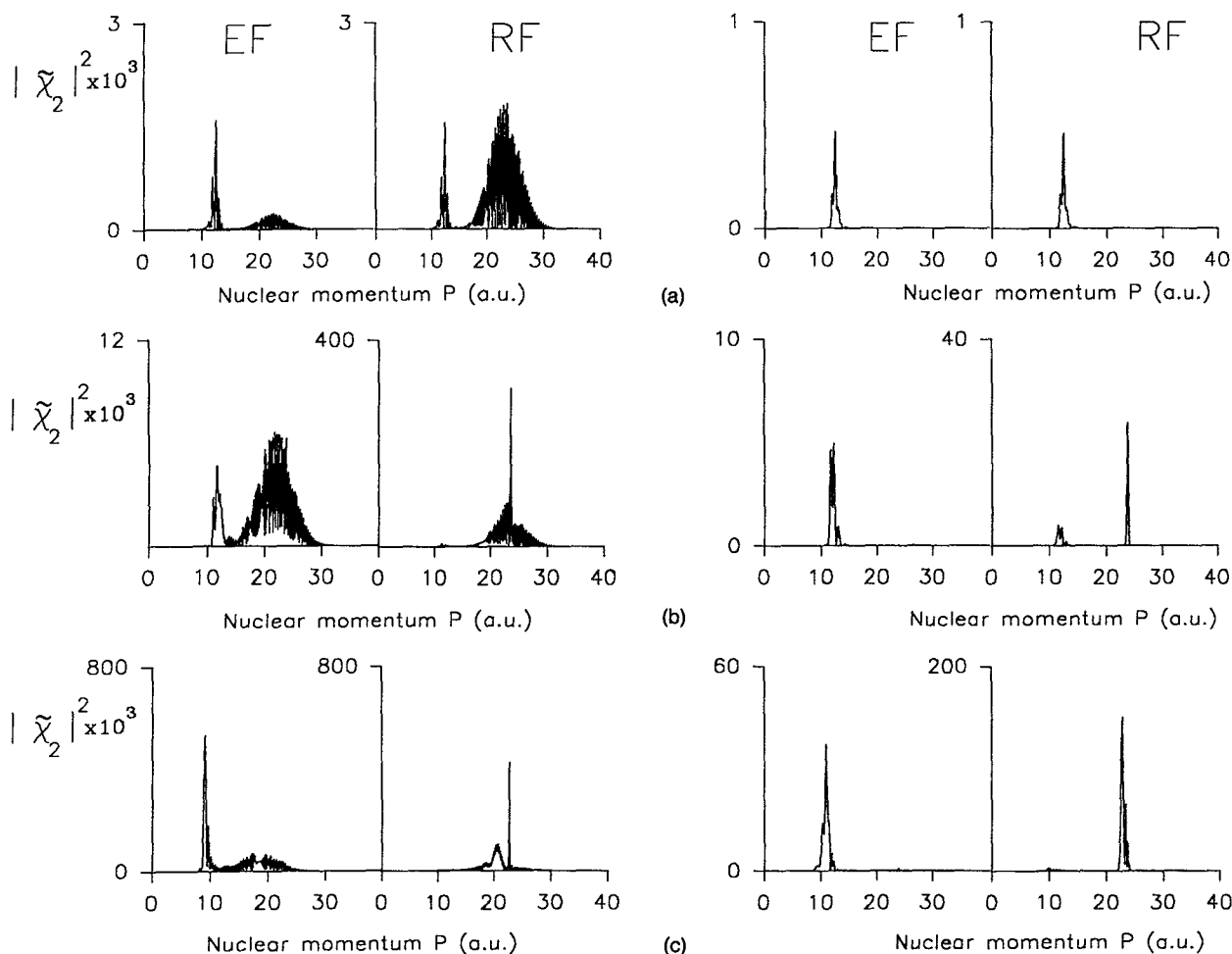
FIG. 10. Asymptotic momentum distributions $|\tilde{\chi}_2(P,\infty)|^2$ supported by the excited-state manifold, resulting from the excitation by a rectangular pulse (left panels) or a Gaussian pulse (right panels) of 50 fs duration and peak intensity (a) $I=10^{12}$ W/cm$^2$, (b) $I=5.6\times10^{13}$ W/cm$^2$, and (c) $I=3.5\times10^{14}$ W/cm$^2$. In each panel, the gauge employed is indicated explicitly.

totic momentum distribution $\tilde{\chi}_2(P,\infty)$ also exhibits a noticeable one-photon peak only at low intensity. As suggested by the spectra for the EF gauge which are always dominated by a one-photon peak, this mechanism is also more favored in the EF gauge than in the RF gauge. In the vicinity of $R_e$, where the deceleration action of the ground-state attractive potential is most effective, the interaction potential $V_{12}^{RF}$ in the RF gauge is indeed three times larger than the corresponding potential $V_{12}^{EF}$. In fact, $V_{12}^{EF}$ remains lower than $V_{12}^{RF}$ as long as $R$ does not exceed $R_x$, where the two forms of interaction deliver the same values for the channel coupling potential. Past this point, $V_{12}^{RF}$ decreases while $V_{12}^{EF}$ increases rapidly so that, in the EF gauge, an amplitude localized in the region $R>R_x$ of the ground potential would feel an up-pumping rate which dominates the decelerating or accelerating action of this potential. Thus, a lower bound for the average momentum of the excited wave packet is set by the dressed-picture one-photon crossing point $R_x$ across which $V_{12}^{EF}$ changes its character, switching from a low effective intensity regime prevailing at $R<R_x$ to a high intensity regime at $R>R_x$.

When the up pumping of local amplitudes supported

by the ground potential is faster than the decelerating action of this attractive potential, as occurs at high intensity in the RF gauge, the promoted wave packet feels no net decelerating effects. In this case, a full acceleration accompanying the propagation of the wave packet towards the dissociative asymptote of the upper channel leads to a structure in the momentum distribution at the three-photon position. As the excited wave packet crosses the one-photon resonance position $R_x$, carrying by then a momentum corresponding to a kinetic energy equal to $3\hbar\omega-\epsilon_2(R_x)=2\hbar\omega-\epsilon_1(R_x)$, a one-photon resonant transition may transfer part of the amplitude to the ground-state manifold. Since this amplitude is in the dissociative continuum of this manifold, it is fully accelerated to yield an asymptotic ground state momentum distribution which exhibits a peak at the two-photon position. Typical examples of this situation are given by the cases of the Gaussian and rectangular 20 fs pulses in the RF gauge and at the highest intensity, Fig. 9(c). This full acceleration mechanism is the opposite of the first mechanism which involves a deceleration of the excited wave packet during its transit on the lower channel. It is favored at high intensity, and, for a
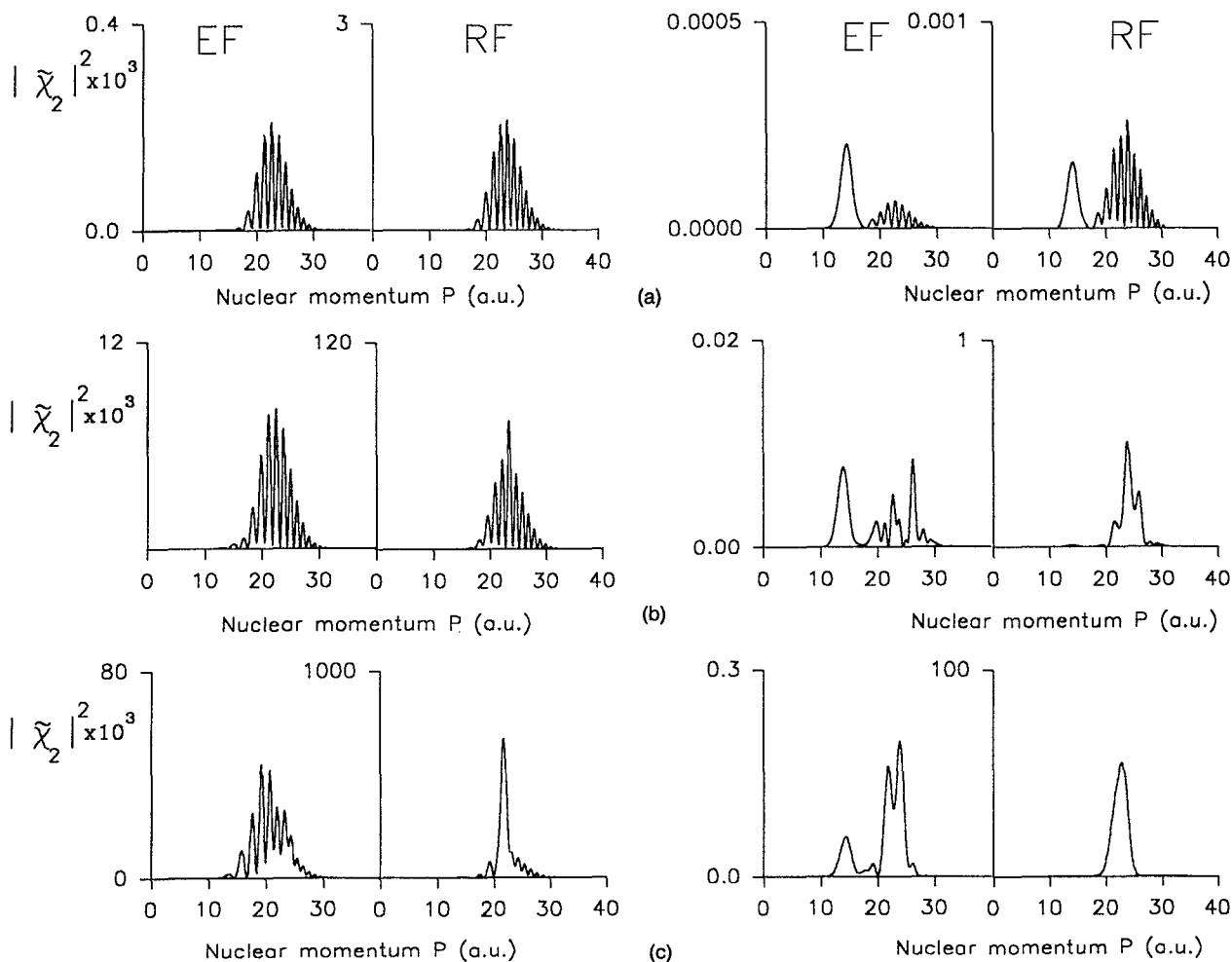
FIG. 11. Asymptotic momentum distributions $|\tilde{\chi}_2(P,\infty)|^2$ supported by the excited-state manifold, resulting from the excitation by a rectangular pulse (left panels) or a Gaussian pulse (right panels) of 5 fs duration and peak intensity (a) $I=10^{12}$ W/cm$^2$, (b) $I=5.6\times10^{13}$ W/cm$^2$, and (c) $I=3.5\times10^{14}$ W/cm$^2$. In each panel, the gauge employed is indicated explicitly.

given intensity, is also more favored in the RF gauge than in the EF gauge. This is confirmed by the spectra in Figs. 9 and 10. Note that a full acceleration is observed in all the spectra of Fig. 11 including those associated with the EF gauge. This can be understood by recalling that the pulses considered in this figure are very short. During the 5 fs pulse duration, much less acceleration or deceleration of the wave packets by the potentials occured and the only acceleration which is observed in all cases is due to the propagation of the promoted wave packet on the upper channel after the laser field had been switched off.

The two mechanisms proposed above can be used to analyze the time-resolved details of the wave packets dynamics shown in Figs. 2–7. As an example, consider the highest intensity illustrated in Figs. 2–5. For the two pulses in the RF gauge, the ground-state coordinate-space wave functions in Figs. 2(b) and 2(d) have gained amplitude at $R > R_x$ starting at $t=5$ fs. This amplitude clearly results from a transfer from the upper channel by a one-photon stimulated emission process which is resonantly enhanced at $R_x$.[16,17] It carries a momentum component which indicates that the previously promoted wave packet is being

fully accelerated. The momentum space upper-channel wave function at 5 fs in Fig. 5(b) and at 10–15 fs in Fig. 5(d) confirm this interpretation. Note also the newly excited $P=0$ component in $\tilde{\chi}_2(P,t)$ at $t=20$ fs, i.e., at the end of the rectangular pulses considered in the panel (d) of Figs. 5–7. As the field has been switched off after this time, this component is later fully accelerated and asymptotically interferes with the components that were previously accelerated to $P=24$ a.u. on the upper channel. No such excitation occurs at the end of the Gaussian pulse since the field intensity is then strongly reduced by the pulse envelope. For this reason, the three-photon peak in the panel (b) of Figs. 5 and 6 does not exhibit an interference pattern. In the EF gauge, a quenching of the accelerated component of the upper-state amplitude appears operative at short times, which can be seen by comparing the $\tilde{\chi}_2(P,t)$ graphs at $t=5$ and 10 fs in Figs. 5(a) and 5(c) with the corresponding graphs in Figs. 5(b) and 5(d). This indicates the onset of the first mechanism discussed above and leads to a peak at the one-photon position in the associated asymptotic spectra. The effect appears more pronounced in Fig. 5(a), corresponding to the Gaussian pulse, than in

Fig. 5(c) corresponding to a rectangular pulse, which still exhibits a relatively strong fully accelerated component at $P = 24$ a.u. The same observation can be made in Figs. 6 and 7. In panel (c) of Fig. 6, the newly formed $P = 0$ component at $t = 20$ fs is subsequently fully accelerated in field-free condition to give a strong enhancement of the three-photon structure. The same effect is weaker in Fig. 7(c) because the lower intensity is less efficient in creating a $P = 0$ component on the excited-state manifold by the promotion of the $v = 0$ vibrational amplitude which remains the dominant feature on the ground-state manifold at the end of the pulse. In Fig. 5(c), this effect is also weaker. However, in this case, the higher intensity has caused a stronger depletion of the $v = 0$ ground vibrational amplitude so that what remains of this amplitude at the end of the pulse is much smaller and the $P = 0$ component newly promoted on the excited-state manifold at this time is weaker.

The wave packet interpretation in the present work is markedly different from the interpretation using the dressed-molecule level scheme. While transitions between the two channels corresponding to absorption and stimulated emission of photons are acknowledged to be continuously operative, they are not considered to be solely responsible for the acceleration and deceleration of the wave packet as evoked elsewhere essentially on the basis of energy conservation in the dressed system.[24] Also, no attempt needs to be made to identify the photon content of these transitions except at the very early stage of the dynamics where the initial promotion of the ground $v = 0$ vibrational state to the excited-state manifold is characterized as a one-photon process instead of a three-photon process.

Note that the two-channel model Hamiltonians associated with $V_{12}^{RF}$ and $V_{12}^{EF}$ are not unitarily equivalent. Moreover, the so-called RF gauge interaction potential $V_{12}^{RF}$ defined by Eqs. (2) and (3) is strictly valid in the case of a cw field only because the relation

$$E = -\frac{1}{c}\dot{A} \leftrightarrow |E_0| = \frac{\omega}{c}|A_0|$$

implicitly used in this definition is appropriate only for an unmodulated periodic field. Thus, in the strictest sense, the above comparisons between the so-called EF and RF gauges should be considered merely as a comparison between two alternative forms of the interchannel couplings. The markedly different behaviors of these two forms of the channel coupling with respect to the internuclear distance has allowed local intensity effects to be delineated. The two extreme acceleration mechanisms proposed previously are differentiated by subtle variations in these local effects and their interplay with the local mechanical properties of the field-free potentials.

The difference observed in the behavior of the system according to whether the laser-induced channel interaction is described in the EF or the RF gauge may reflect the inadequacy of the two-channel description to model realistically the interaction of this ionic system with a strong laser field. Unlike the two-channel problems considered presently, the infinite-channel time-dependent problems

defined by an electronic-field interaction in length form, $\mu.E$, and in velocity form, $A.p$, respectively, are connected by a proper unitary transformation. Thus, gauge invariance requires a description which does not involve a truncation of the Hamiltonian to a finite number of field-free BO channels. Work in this direction is currently in progress in our laboratory and uses a time-dependent *ab initio* adiabatic representation previously defined in a formal manner for Coulomb systems driven by an arbitrarily shaped laser pulse.[36]

[1] T. S. Rose, M. J. Rosker, and A. H. Zewail, J. Chem. Phys. **88**, 6672 (1988); M. J. Rosker, T. S. Rose, and A. H. Zewail, Chem. Phys. Lett. **146**, 175 (1988).

[2] A. H. Zewail, Science **242**, 1645 (1988).

[3] J. Misewich, J. H. Glownia, J. E. Rothenberg, and P. P. Sorokin, Chem. Phys. Lett. **150**, 374 (1988).

[4] D. J. Tannor and S. A. Rice, J. Chem. Phys. **83**, 5013 (1988).

[5] S. Shi and H. Rabitz, J. Chem. Phys. **92**, 364 (1990); S. Shi, A. Woody, and H. Rabitz, *ibid.* **88**, 6870 (1988).

[6] N. M. Kroll and K. M. Watson, Phys. Rev A **13**, 1018 (1976).

[7] A. M. F. Lau, Phys. Rev. A **13**, 139 (1976); A. M. F. Lau and C. K. Rhodes, *ibid.* A **15**, 1570 (1977); *ibid.* **16**,2392 (1977).

[8] T. F. George, J. Phys. Chem. **86**, 10 (1982); T. F. George, I. H. Zimmerman, J. M. Yuan, J. R. Laing, and P. L. DeVries, Acc. Chem. Res. **10**, 449 (1977).

[9] M. Shapiro and M. Bony, J. Chem. Phys. **83**, 1588 (1985).

[10] A. D. Bandrauk and M. L. Sink, J. Chem. Phys. **74**, 1110 (1981); A. D. Bandrauk and G. Turcotte, J. Phys. Chem. **85**, 3039 (1985); A. D. Bandrauk and O. Atabek, *Advances in Chemical Physics*, LXXIII, edited by J. O. Hirschfelder, R. E. Wyatt, and R. D. Coalson (Wiley, New York, 1989), Chap. XIX, p. 823.

[11] T. T. Nguyen-Dang and A. D. Bandrauk, J. Chem. Phys. **74**, 3256 (1983); *ibid.* **80**, 4926 (1984); A. D. Bandrauk and T. T. Nguyen-Dang, *ibid.* **83**, 2840 (1985).

[12] T. T. Nguyen-Dang and A. D. Bandrauk, J. Chem. Phys. **85**, 7224 (1986); T. T. Nguyen-Dang in *Atomic and Molecular Processes with Short Intense Laser Pulses*, edited by A. D. Bandrauk, (Plenum, New York, 1988), pp. 323.

[13] J. F. McCann and A. D. Bandrauk, J. Chem. Phys. **96**, 903 (1992).

[14] S. I. Chu, *Advances in Chemical Physics*, LXXIII, edited by J. O. Hirschfelder, R. E. Wyatt, and R. D. Coalson (Wiley, New York, 1989), Chap. XVII, p. 739.

[15] X. He, O. Atabek, and A. Giusti-Suzor, Phys. Rev. A **38**, 5586 (1988); *ibid.* **42**, 1585 (1990).

[16] R. W. Heather, Comput. Phys. Commun. **63**, 446 (1991).

[17] R. W. Heather and F. H. Mies, Phys. Rev. A **44**, 7560 (1991).

[18] H. P. Breuer and M. Holthaus, Z. Phys. D: **11**, 1 (1989).

[19] H. P. Breuer, K. Dietz and M. Holthaus, J. Phys. B: **24**, 1343 (1991); J. Phys. France **51**, 709 (1990).

[20] T. S. Ho and S. I. Chu, Chem. Phys. Lett. **141**, 315 (1987).

[21] P. H. Bucksbaum, A. Zavriyev, and H. G. Muller, Phys. Rev. Lett. **64**, 1883 (1990).

[22] A. Zavriyev, P. H. Bucksbaum, H. G. Muller, and D. W. Schumacher, Phys. Rev. A **42**, 5500 (1990).

[23] M. Sugawara, M. Kato, and Y. Fujimura, Chem. Phys. Lett. **184**, 203 (1991).

[24] G. Jolicard and O. Atabek, Phys. Rev. A (in press).

[25] E. E. Aubanel, A. D. Bandrauk, and J. M. Gauthier, Phys. Rev. Lett. (submitted).

[26] H. R. Reiss, Phys. Rev. A **19**, 1140 (1979); *ibid.* **22**, 770 (1980).

[27] A. D. Bandrauk, O. F. Kalman, and T. T. Nguyen-Dang, J. Chem. Phys. **84**, 6761 (1986).

[28] T. T. Nguyen-Dang and H. Abou-Rachid, Phys. Rev A **45**, 4752 (1992).

[29] T. T. Nguyen-Dang and H. Abou-Rachid, J. Chem. Phys. **96**, 256 (1992).

[30] T. T. Nguyen-Dang, H. Abou-Rachid, and D. Tanguay, in *Coherence Phenomena in Atoms and Molecules in Intense Fields*, edited by A. D. Bandrauk and S. Wallace (Plenum, New York, 1992).

[31] T. T. Nguyen-Dang, S. Manoli, and H. Abou-Rachid, Phys. Rev. A **43**, 5012 (1991).

[32] T. T. Nguyen-Dang and S. Manoli, Phys. Rev. A **44**, 5841 (1991).

[33] M. D. Feit, J. A. Fleck, Jr., and A. Steiger, J. Comput. Phys. **47**, 412 (1982).

[34] F. V. Bunkin and I. I. Tugov, Phys. Rev. A **8**, 601 (1973).

[35] W. H. Press, B. P. Flannery, S. A. Teukolsky, and W. T. Vetterling, *Numerical Recipes* (Cambridge University, Cambridge, 1986).

[36] T. T. Nguyen-Dang, J. Chem. Phys. **90**, 2657 (1989).